

Skin feature tracking using deep feature encodings

Jose Ramon Chang, MSc¹ and Torbjörn E. M. Nordling, MSc, PhD^{1,2*}

¹Department of Mechanical Engineering
National Cheng Kung University
Tainan 701, Taiwan

²Department of Applied Physics and Electronics
Umeå University
90187 Umeå, Sweden

{jose.chang, torbjörn.nordling}@nordlinglab.org

Abstract

Facial feature tracking is a key component of imaging balistocardiography (BCG) where accurate quantification of the displacement of facial keypoints is needed for good heart rate estimation. Skin feature tracking enables video-based quantification of motor degradation in Parkinson's disease. Traditional computer vision algorithms include Scale Invariant Feature Transform (SIFT), Speeded-Up Robust Features (SURF), and Lucas-Kanade method (LK). These have long represented the state-of-the-art in efficiency and accuracy but fail when common deformations, like affine local transformations or illumination changes, are present.

Over the past five years, deep convolutional neural networks have outperformed traditional methods for most computer vision tasks. We propose a pipeline for feature tracking, that applies a convolutional stacked autoencoder to identify the most similar crop in an image to a reference crop containing the feature of interest. The autoencoder learns to represent image crops into deep feature encodings specific to the object category it is trained on.

We train the autoencoder on facial images and validate its ability to track skin features in general using manually labeled face and hand videos. The tracking errors of distinctive skin features (moles) are so small that we cannot exclude that they stem from the manual labelling based on a χ^2 -test. With a mean error of 0.6-4.2 pixels, our method outperformed the other methods in all but one scenario. More importantly, our method was the only one to not diverge.

We conclude that our method creates better feature descriptors for feature tracking, feature matching, and image registration than the traditional algorithms.

Keywords: feature tracking, feature matching, image registration, autoencoder, Lucas-Kanade method, SIFT

1 Introduction

Facial feature points are distinctive points typically located around the eyes, nose, chin, and mouth that carry the most relevant information for both discriminative and generative purposes (Wang et al., 2018). With increasingly larger and broadly available facial imagery datasets, researchers have used deep learning to teach computers to perform interesting tasks, such as using these feature points to determine the level of drowsiness/sleepiness of a driver (Garcia et al., 2012), recognize emotions (Zhao et al., 2016), quantify fatigue (Uchida et al., 2018), estimate heart rate (Hassan et al., 2017), and lip-reading (Chung et al., 2017).

Feature tracking can be achieved through iterative feature matching across sequential frames in a video. Current feature matching and tracking methods are not robust enough, failing sometimes even from small photometric/geometric changes, motion deformations, or occlusions present in the data as we demonstrate. We define feature matching as the task of, based on information about the feature in one image, finding the same feature in another deformed image. A feature,

in this case, is any characteristic that is a part of the main entity/object portrayed in the image. While an object constitutes a whole on its own with a boundary separating it from other objects and distinguishing it from its environment, e.g. a car on the street or a bear in a forest, a feature is a part of an object and does not have a boundary. A feature is defined by a local pattern of some sort, e.g. a wrinkle on skin, and it is typically hard to even say where it ends. This makes it significantly harder to define, detect, match, and track features compared to objects. Nonetheless, feature matching is sometimes treated as an object detection/recognition task. In general, the real world performance of tracking methods decreases with the number of assumptions made in the method. These assumptions include but are not limited to; small motion, specific types of geometric deformations, constant lighting, corner points, and no occlusion of points. Tracking of the position of a skin region of interest is particularly challenging. In an image, skin typically appears homogenous with only some irregularly spaced locally distinct features. The pattern of these locally distinct features may be heavily deformed due to change in facial expression or lighting. Some skin features are though unique and easily recognisable by the human eye, e.g. a mole or birth mark. To track these feature points, here we follow the established engineering practice of applying the simplest method proven to work in other applications. Therefore, we use deep learning, more precisely an autoencoder, to track crops containing these distinct skin feature points, aiming to push the limits of current computer vision methods by creating a more robust, and accurate pipeline to track skin feature points.

While SIFT (Lowe, 2004) and SURF (Bay et al., 2006) have been invented almost 20 years ago, they are still considered by many to be state-of-the-art feature matching techniques. One research group found SIFT to be the second-best descriptor in terms of feature matching and recognition accuracy of the same object or scene (Mikolajczyk and Schmid, 2005). Gradient Location and Orientation Histogram (GLOH), their proposed extension of SIFT, marginally outperformed SIFT for most tasks. This shows the robustness and distinctiveness of SIFT descriptors. A review found that SIFT and SURF converged similarly to the lowest errors for monocular visual-odometry tasks (Chien et al., 2016). Another group concluded that SIFT is still the most accurate feature descriptor for image recognition and feature matching applications (Khan et al., 2015). They also found that general-purpose feature descriptors perform fairly well for feature matching but are not good for image recognition. Some researchers compared SIFT descriptors with descriptors obtained using a pre-trained Convolutional Neural Network (CNN) on the Imagenet dataset (Zheng et al., 2017). They found that while CNN-based methods have advantages in nearly all their benchmarking datasets, SIFT is still better in the cases where images are gray-scale, there are intense color changes, and when there are severe occlusions. One review concluded that SIFT is the most accurate feature-detector-descriptor for overall scale, rotations, and affine deformations (Tareen and Saleem, 2018). We think this is due to the CNN not having these types of instances in its training distribution. In the past 2 years, SIFT and SURF have been used in many applications, like underwater image recognition for autonomous underwater vehicles (Ansari, 2019), image forgery

*Corresponding author

detection (Alberly et al., 2018; Chen et al., 2019), and mosaicking of unmanned aerial vehicle images for crop growth monitoring (Zhao et al., 2019). In 2017, SIFT was even used for currency recognition (Doush and Sahar, 2017).

By far, the most commonly used method for sparse optical flow is LK (Lucas and Kanade, 1981). This method is mathematically well defined and has clear assumptions for proper functioning like no photometric deformations, small displacement (or the images are separated by a very small time increment), and the point is a corner. Since this method is computationally cheap, it can be applied in many real-time feature tracking applications. Within the last 5 years applications of LK include image alignment (Chang et al., 2017), image registration (Douini et al., 2017a), feature tracking (Ahmine et al., 2019; Douini et al., 2017b), visual odometry (Wong and Majji, 2017), and motion breath recognition (Tran et al., 2018). In 2015, this method was used for facial expression recognition (Pu et al., 2015).

1.1 Deep learning for skin feature tracking

Deep learning has been extensively used in medical applications involving skin. Recent reviews include deep learning for remote photoplethysmography (rPPG) (Ni et al., 2021; Cheng et al., 2021a), gaze estimation (Cheng et al., 2021b), speech recognition (Lee et al., 2021), skin lesion segmentation (Stofa et al., 2021), and driver fatigue detection (Sikander and Anwar, 2018). Although all of these implicitly require skin feature tracking, there has been little original research done on quantifying the matching error of skin features explicitly. The most similar research that we could find to ours is of a group that tried to match keypoints on the back of patients using hyperspectral images (Manni et al., 2020). Their hyperspectral camera, running at 16 FPS, acquired 41 equally distributed spectral bands in the range of 450-950 nm in one snapshot of size 2048×1080 . A color image is used as a reference to register all the hyperspectral data, ensuring proper data fusion. This yields a tensor of size $1080 \times 2048 \times 41$ to which they then later applied the Saliency-Band-Based Selection algorithm (SSBS) (Su et al., 2018) to reduce its dimensions. They aim to find the correspondences of points on the back of 17 patients with images taken when they breathe in and out. They applied SURF and DEep Local Feature (DELf) to create feature descriptors of keypoints in the images. Their results indicate that DELf had a localization error of 0.25 mm and that it outperformed the SURF descriptors with respect to the ground truth based on optical markers. As explained in detail later, DELf implicitly select features and cannot be used to track a selected feature like in our case.

1.2 Autoencoders for feature matching

The most popular learning paradigm in computer vision, and all fields in general, is supervised learning Chum et al. (2019); Khan et al. (2021). However, a common bottleneck factor when training a supervised learning model is the amount of good-quality sample-label pairs. The same complexity that allows these models to learn very complex functions is also responsible for them requiring vast amounts of data to tune this extensive amount of parameters.

An autoencoder is a type of neural network that aims to learn the identity function. As such, it can be trained by minimizing the discrepancy or distance between the original data and its reconstruction. This means that it only requires samples for its training and removes the need for labels. The identity function may seem a trivial, meaningless function to learn. However, if we constrain the latent space to have fewer dimensions than our input, then we force the network to learn the most salient, distinctive features of our data. Their use for dimensionality reduction was popularized in 2006 (Hinton and

Salakhutdinov, 2006). They described the algorithm as a nonlinear generalization of Principal Component Analysis (PCA). Similarly to PCA, a key feature of autoencoders is that they are able to encode the input data into latent state representations that provide interesting insight into the samples of the data. It is described as a nonlinear generalization of PCA because a neural network typically passes the output of each neuron through a nonlinear function, *e.g.* sigmoid, tanh, Rectified Linear Units (ReLU), or all of the ReLU variants.

Autoencoders have been used for feature matching in the past. A siamese network was used by researchers to match the latent space representation of tops and bottoms from the FashionVC and MbFashion (Gao et al., 2019). They used the outfits the fashionistas published on different social networks as their ground truths. Another team used a convolutional autoencoder to match image patches between two infrared images for 3D reconstruction (Knyaz et al., 2017). Their results indicate that their autoencoder was better for matching the features of the test part of their Multi-View Stereo InfraRed (MVSIR) imagery dataset compared to SIFT (Lowe, 2004), deep convolutional feature point descriptors (Simo-Serra et al., 2015), and stereo matching convolutional neural network (Zbontar and LeCun, 2016). They mentioned that if the convolutional autoencoder is able to obtain good restoration quality then it has learned to extract the most salient information from the data. Thus the hidden representations can be used for sparse image matching. Another group used a convolutional autoencoder to learn features from images of finger veins and then used a support vector machine (SVM) to classify them (Hou and Yan, 2019). They credited the convolutional autoencoder for effective learning of finger vein features, preserving the main information of the image, reducing redundant information, and improving the recognition efficiency with the help of their SVM classifier. We train our autoencoder to match skin features in general.

1.3 Deep learning for feature tracking

1.3.1 Object detection based tracking

Most deep learning feature tracking research is built upon the simple task of object detection. Object detection is one of the most elementary problems in computer vision where one seeks to locate object instances from a set of predefined categories in images (Liu et al., 2020). An object detection network takes the image as input and outputs a set of bounding boxes. Each of these bounding boxes is typically defined by its x and y coordinates, box width and height, confidence that there is an object inside, and the probability of that object being from each one of the predefined classes.

Many deep learning approaches for Multiple Object Tracking (MOT), also known as Multi-Target Tracking, have been published in the last four years (Ciaparrone et al., 2020). Similar to object detection, MOT assigns bounding boxes to the detected objects but in addition, each bounding box is associated with a target ID. This target ID serves to differentiate among intra-class objects.

The standard approach of most MOT algorithms is referred to as “tracking-by-detection”, *i.e.* the tracking is done by iteratively detecting objects successively across the frames of a video. The bounding boxes of two successive frames are usually associated together to assign the same target ID to the bounding boxes that contain the same object. Recently, many methods that have been developed can detect objects with very good accuracy and precision, *e.g.* Faster-Region based Convolutional Neural Networks (RCNN) (Ren et al., 2015), Single Shot Detector (Liu et al., 2016), You Only Look Once (YOLO) (Redmon et al., 2016), YOLO v2 (Redmon and Farhadi, 2017), YOLO v3 (Redmon and Farhadi, 2018), YOLO v4 (Bochkovskiy et al., 2020), Mask RCNN (He et al., 2017a), and Region-based Fully Connected Networks (R-FCN) (Dai et al., 2016). Since these methods can already provide very good detections, most of these algorithms focus on developing better associating algorithms to track objects with the same target ID. These algorithms are developed for large objects,

e.g. a pedestrian, while we aim to track small objects with low resolutions, *e.i.* skin features. This makes our problem inherently more difficult as we have less local information and less distinctive features (patterns/ structures) to identify our target in the images; leading to a possible increase in false positive cases as there could be many parts of the image with a similar appearance.

The most common deep learning algorithms for detection are variants of Faster-RCNN (Ren et al., 2015) or Single-Shot Detection (SSD) (Liu et al., 2016). While these algorithms have shown to be very accurate at tracking objects, most of these deep learning methods require large amounts of labeled data to train the detector. Labeling data is usually strenuous labor, as accurate training labels require the use of a consensus label of many labeling attempts. This data restraint is a hallmark of supervised learning. The parameters of the model are updated based on the gradients of the error between the prediction and ground truth. In addition, they are still slow and do not meet real-time requirements (Bi et al., 2019). Here we use an autoencoder to avoid the labelling issue.

Centernet (Zhou et al., 2019) is another object detection algorithm that represents objects as the center of their bounding box. Object size, dimension, 3D extent, orientation, and pose are then regressed directly from image features at these center locations. Their best model, which is based on Hourglass-104 (Law and Deng, 2018), is trained to produce heatmaps where peaks correspond to object centers. It achieves 42.2% Average Precision (AP) in 7.8 FPS in the Microsoft (MS) Common Objects in Context (COCO) (Lin et al., 2014). While this is comparable to other state-of-the-art object detectors like FasterRCNN (Ren et al., 2015), YoloV3 (Redmon and Farhadi, 2018), and RetinaNet (Lin et al., 2017b), it differs significantly from our applications as its more similar to object detection than feature matching. An object recognition algorithm aims to identify the main object in the image. It does so by predicting a probability distribution of all the object categories it has been trained to recognize. An object detection algorithm aims to, in addition to recognizing which are the objects in the image, locate all the main objects by estimating their bounding box locations and dimensions.

1.3.2 Other deep learning based tracking

Deepflow (Weinzaepfel et al., 2013) is a variational approach that uses a CNN to calculate the dense optical flow between two images. Variational approaches had been widely used ever since their invention in 1981 (Horn and Schunck, 1981). They use a 6-layered convolutional architecture to create descriptors between images and retrieve quasi-dense correspondences based on these feature descriptors. Their claim for being able to deal with large motions comes from their performance on the Middlebury (Baker et al., 2011) and MPI-Sintel (Butler et al., 2012) datasets. These datasets are well-known in the optical flow community. However, the Middlebury dataset has less than 3% of its pixels with displacements over 20 pixels and none have displacements over 25 pixels. The MPI-Sintel dataset contains approximately 10% of its pixels with a displacement of over 40 pixels. These displacements are still small for our applications. In addition, while they use convolutional layers and max pooling, there is no learning done by the network and all of its kernel parameters are predetermined.

FlowNet (Dosovitskiy et al., 2015) was one of the first attempts to train a deep CNN to estimate optical flow in an end-to-end manner. They developed FlowNetSimple and FlowNet-Corr. FlowNetSimple takes as input both images stacked together and tries to predict the optical flow map. FlowNetCorr takes each image as a separate input, processes them, and then uses a correlation layer to identify correspondences between the processed maps. Both networks aim to minimize the endpoint error, which is the Euclidean distance between the predicted flow vector and the ground truth. They mentioned that the amount of frames with ground truth in the Middlebury, Sintel, and Karlsruhe Institute of Technology and Toyota Technological Institute (KITTI) (Geiger et al., 2013) datasets is too small for training a deep CNN. They resorted to creat-

ing a dataset called Flying Chairs consisting of 22,872 frame pairs with their respective ground truth. They show that both FlowNet models outperform other architectures in the Flying Chairs dataset but struggle in other datasets. The authors believe that FlowNetCorr can learn the features better and can outperform all other methods if trained on a realistically large dataset.

DELf (Noh et al., 2017) is a method to calculate feature descriptors of image patches and keypoint selection. It uses the convolutional layers of ResNet-50 to reduce the input image into feature maps of 1024 channels. These are then assigned attention scores to select the spatially most distinctive features of the image. The added attention layer was trained using images of the Google-Landmarks (Zheng et al., 2009) dataset by minimizing the cross entropy loss of the predicted class and its true label. The dimensionality of the selected keypoints was later reduced to 40 dimensions using Principal Component Analysis (PCA). They tested this algorithm on image retrieval of this dataset. Its area under the precision-recall curve outperformed other state-of-the-art feature descriptors like Deep Image Retrieval (DIR) (Gordo et al., 2016) and CONGAS (Neven et al., 2008). One of the main drawbacks of this method is that the granularity of positions of keypoints is effectively determined by the feature map before the attention layer. In other words, one can not calculate the descriptors of an exact location (x, y) of a keypoint in the original image.

Detector-Free Local Feature Matching with Transformers (LoFTR) (Sun et al., 2021) is an algorithm inspired by SuperGlue (Sarlin et al., 2020). Like Scross-attention self and cross attention to find correspondences between keypoints. The main difference between these two is that LoFTR does not require a detector and does pixel-wise dense matching at a coarse level and refining the good matches at a fine level. Similarly, they require a method to obtain the descriptors of keypoints. In their experiments, they used Feature Pyramid Networks (Lin et al., 2017a) (FPN) to obtain feature maps at multiple levels from the images. FPN tries to build feature pyramids whose layers at all levels are equally semantically strong. It does this by nearest neighbor upsampling from the lowest level of the pyramid of a traditional CNN. This approach has been shown to improve the AP performance of the Faster R-CNN (Ren et al., 2015) over its original backbone on the COCO dataset. However, both LoFTR and FPN address the feature matching problem from a different perspective than ours. FPN creates feature maps from an entire image which could contain multiple objects of different sizes and classes. We aim to create an algorithm that, given a crop of an image with a feature/keypoint at its center, creates the most distinctive representation from all other possible crops. It is worth noting that, to the extent of our knowledge, none of the feature constructors aim to build representations of features representing a part of an object. Since an object is a dominant element in an image, it typically has textures, color changes, gradients, and shapes that make it significantly more distinctive than its surroundings. In our case, we would like to distinguish between features of the same domain, *e.g.* a wrinkle edge, a hair, a mole, from other skin features in an image whose object is a face (imaging BCG) or a hand (tremor quantification of PD patients). This makes our problem inherently more difficult. LoFTR is a matching algorithm based on these feature pyramids, which is an entirely different part of the feature matching pipeline.

SuperGlue (Sarlin et al., 2020) is a graph neural network that can find matches between two sets of features by jointly finding correspondences and rejecting non-matchable points. It is a transformer (Vaswani et al., 2017) based graph neural network that uses intra-image (self) and inter-image (cross) attention to understand the appearance of keypoints and the spatial relationships between them; respectively. This algorithm takes as input the position and detection confidence of the keypoints in two images along with their respective descriptors and tries to find associations between them. While efficient and precise matching of keypoint pairs is essential in a feature-matching algorithm, our application focuses on the learning and formulation of feature representations.

2 Materials and Methods

Feature tracking can be simplified into doing feature matching successively for all frames in a video. We want to compare the feature description ability and matching of different algorithms: SIFT, SURF, LK, and our Deep Feature Encodings (DFE). For a full schematic of the flow of our experiments see Figure 1. We decided to track two face features, under two different motion conditions, and one hand feature of a patient with Parkinson’s disease (PD) performing a postural tremor test. The facial features we decided to track are a face mole and a nose tip and the hand feature is a mole, see Figure 2. These are visible in every frame in our validation dataset.

We used the default implementation of SIFT in Open CV, *i.e.* the 128-feature descriptor. We expanded SURF to use rich descriptors (128-feature descriptor). For LK we used the pyramidal implementation using a 10×10 window and a 4-leveled pyramid. For the DFE method, we constrained the autoencoder to a compression factor of 0.0444 (128 latent variables) using $31 \times 31 \times 3$ crops as input. Skin is rather homogeneous with distinct features in some places. We, therefore, want to be able to select an area of distinct features to track, which is why it makes sense to work with patches.

The task is to match a reference point from the first frame of the video (either face mole, nose tip, or hand mole) in every subsequent video frame. For SIFT, SURF, and DFE; a match is made between the pair of descriptors h that minimize the Sum of Squared Residuals (SSR),

$$SSR = \sum (h_{\text{predicted}} - h_{\text{reference}})^2,$$

where $h_{\text{predicted}}$ is the descriptors of a potential match in the second image and $h_{\text{reference}}$ is the descriptor of the feature we want to track. Both must be produced using the same method. The matching strategy of DFE is shown in Figure 3. For LK, the match is simply the point that minimises, in a least-squares sense, the optical flow equations. Only DFE uses color information, coded in the CIELAB color space. SIFT, SURF, and LK all use images in grayscale.

To evaluate the matching error of the methods, the images were manually labeled with pixel-level accuracy. A Chi-square analysis was performed on the differences of the x and y coordinates in a series of relabeling attempts for a subset of the validation images to estimate the labelling error and assess the errors of the methods.

2.1 Training dataset

The training data for the autoencoder of our DFE method is the University of Tennessee, Knoxville Face (UTKFace) dataset. UTKFace is a large-scale face dataset with a long age span (range from 0 to 116 years old) (Zhang et al., 2017). It consists of 24,108 face images in the wild of humans of varying sex, age, and ethnicity, see Figure 15.

All the wild face images are RGB color-coded but were converted into the CIELAB color space (McLaren, 1976). The CIELAB color space aims to be perceptually pseudo uniform. Large differences in the color representations represent large color changes as perceived by humans. The transformation from RGB to CIELAB is described in the section CIELAB color space (Appendix A.3).

The images have different backgrounds, lighting, postures, and resolutions. Since the images are collected from the internet, some images seem to be black and white and some include some type of watermark. There is a lot of variety in the face crops as the dataset includes faces with makeup, facial expressions, glasses, facial hair, and other head garments, *e.g.* headbands, hats, bandanas, bindi, and earrings.

To train an autoencoder that is invariant to image scale and specialises in skin features, we have resorted to crops from the original images of the faces to obtain images of different resolutions. We use the OpenCV ResNet-10 based model to detect the faces across all the 24,108 pictures in the UTKface wild faces dataset and select the face with the highest confidence. The results of the face cropping using the ResNet-10 based

model are images of aligned cropped faces with the majority of the image corresponding to face information.

We subsequently, cropped image patches of size $31 \times 31 \times 3$ from all the detected faces with a stride of 30. These cropped patches serve as input for our deep convolutional autoencoder during the training phase. With this partition, we have approximately 1.9 million training crops.

2.2 Validation dataset

The videos we used to test our algorithms are all collected in our lab for two different projects. The data can be divided into the following sets:

1. **Remote ballistocardiography:** This dataset was obtained with the goal of estimating the heart rate remotely by tracking the subtle head movement produced by the blood flowing through the carotid artery. The face videos are recorded in full HD resolution at 50 FPS (1920×1080 pixels) using a Panasonic GX85 with Olympus M.ZUKIO DIGITAL ED 14-150mm F4-5.6II lens (Wang, 2020). These videos were recorded under two motion conditions:

- **Small motion**—The subject is instructed to simply look at the camera for a couple of minutes without moving, referred to as static condition.
- **Large motion**—The subject is filmed while riding an exercise bicycle. The motion is larger than in the static case and periodic. This is referred to as the bike condition.

Both videos show the same subject performing the experiments. The distance-to-pixel ratio was calculated from the physical distance between pupils (mm) and the estimated distance of pupils (pixels) from the first frame in each of the experiments. To estimate the distance of pupils in the images, the two pupils were selected manually and the square root of the L2 norm of their residuals was calculated. The subject has approximately 63 mm of the distance between his pupils. In the static conditions, there are 219.23 pixels between pupils; equating to 0.287 mm/pixel. In the bike conditions, there are 227.06 pixels between pupils; equating to 0.277 mm/pixel.

For the static conditions, the distance between pupils is Face cropping was done by first detecting all faces in the video frames using the Open CV ResNet10 model. The cropping was based on the average bounding box center with width and height scaled at 1.5 times the average width and height of all detected faces across the video frames. This cropping scheme allows us to obtain images of the same size where the face dominates while allowing us to observe the motion of the head in the video.

2. **Parkinson’s disease postural tremor test:** This data set of hands of PD patients has been recorded as a step toward digitalising the Unified Parkinson’s Disease Rating Scale (UPDRS) motor exams. We use this video to evaluate the generalizability of our method to track skin features outside the face. For more information on how the examination was administered see our protocol (Ashyani et al., 2022). The subject was diagnosed with a Movement Disorder Society-Unified Parkinson’s Disease Rating Scale (MDS-UPDRS) score for postural tremor on the left hand of one. From the three available views (front, right, left) we took the left view of the left hand. The hand video is recorded at 240 FPS in HD resolution (1280×720 pixels) using the back camera of a Samsung S7 mobile phone. The area corresponding to the hand was manually cropped using a similar static window approach as for the face dataset, this video is referred to as PD.

Both video datasets were coded in RGB color space but transformed to the CIELAB color space using the algorithm described in section CIELAB color space (Appendix A.3). The videos were also subsampled to 2 FPS to increase the displacement from frame to frame, *i.e.* tracking challenge, and reduce

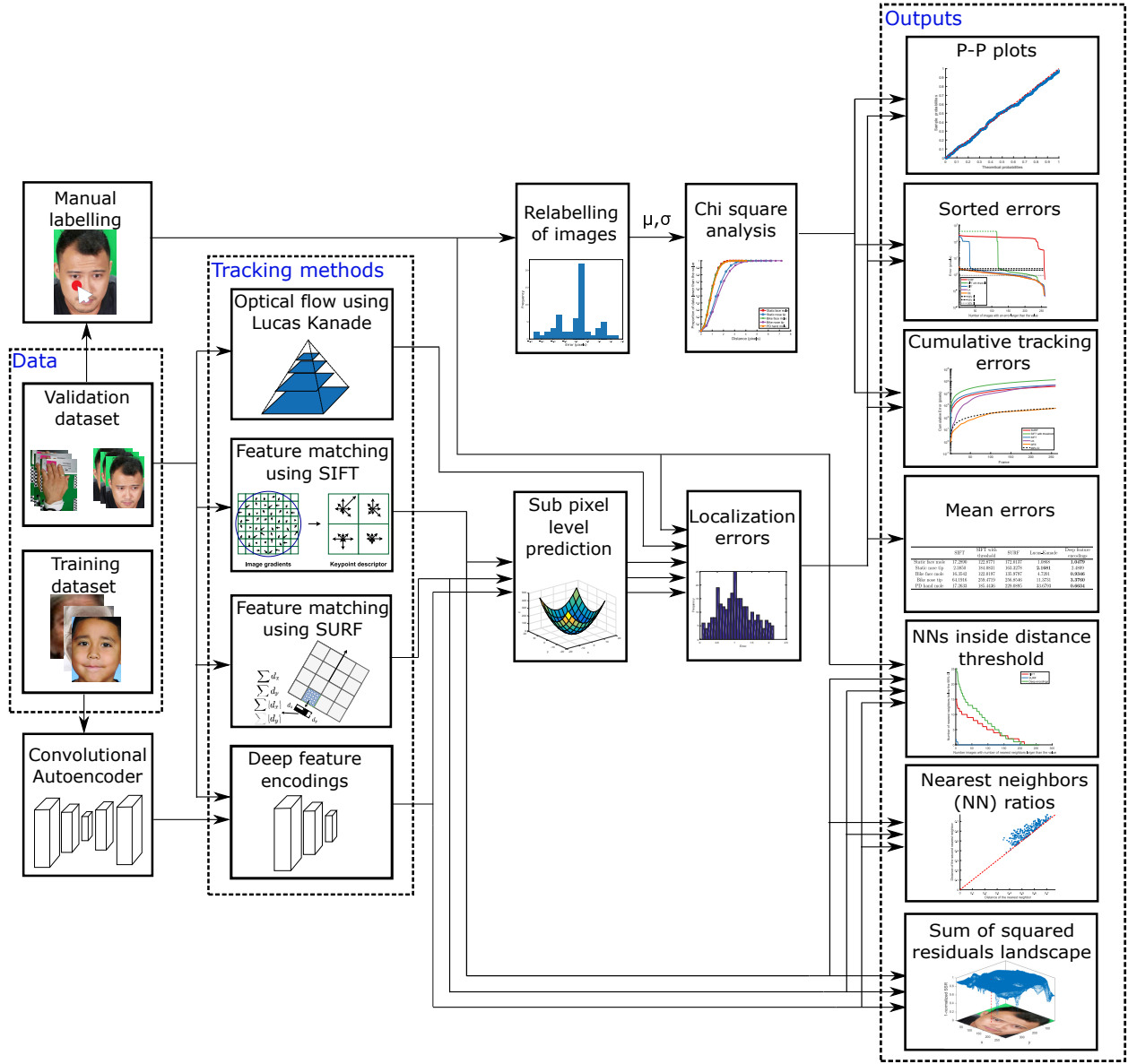


Figure 1: Schematic workflow of our analyses and experiments. The UTKface (training) dataset was used to train the autoencoder used in our DFE method. Our validation dataset was manually labeled to obtain the ground truth of the location of the features. It was relabeled several times and the mean and standard deviations of these localization errors were used to simulate a Chi-square distribution of the labelling errors. The feature tracking methods were used to predict the localization of the skin features in the validation dataset. For SIFT, SURF, and DFE the optimal match is determined to obtain subpixel level predictions before calculating the error relative to the manual labelling. Based on those errors the P-P plots, sorted errors, cumulative tracking errors, and mean errors are reported. The nearest neighbors inside the distance threshold, the nearest neighbors ratios, and the SSR landscape take the high-dimensional representations of the points as input and visualise them.

the computation time. The final frame count for the face videos after temporal subsampling is 261 for the static condition and 170 for the bike condition. For the hand video, the final frame count was 40 frames. The images were reduced to 420×300 pixels to better match the images extracted from the UTKface dataset and to make the evaluation process computationally cheaper.

2.3 Hardware used

The training of the autoencoder was done in an Ubuntu server with an AMD Ryzen Threadripper 1950X 16-core processor with 32 threads and 64 GB of RAM. The system also has three ASUS 1080 Ti GPUs to speed up the parallel computations in the training of the deep neural network.

2.4 Chi-square analysis

A Chi-square analysis was used to establish a threshold for determining which errors were likely a result of human labelling. Errors that are not due to human labelling errors are, by default, attributed to the flaws of the tracking method.

For each body part and motion condition, fifteen images were selected for each skin feature and relabeled five times. These images were equispaced temporally and presented cyclically to the labeller. This was done to prevent the labeller from seeing the same image multiple times in a row. The relabelling was done roughly three months after the original labelling of the images and the labeller was not allowed to take breaks while relabeling each set of 15 images five times. The original labelling was included to obtain a set of 90 samples for each body part and motion condition.

For each relabeling attempt, we computed the error against the mean of all the labeling attempts of the image separately

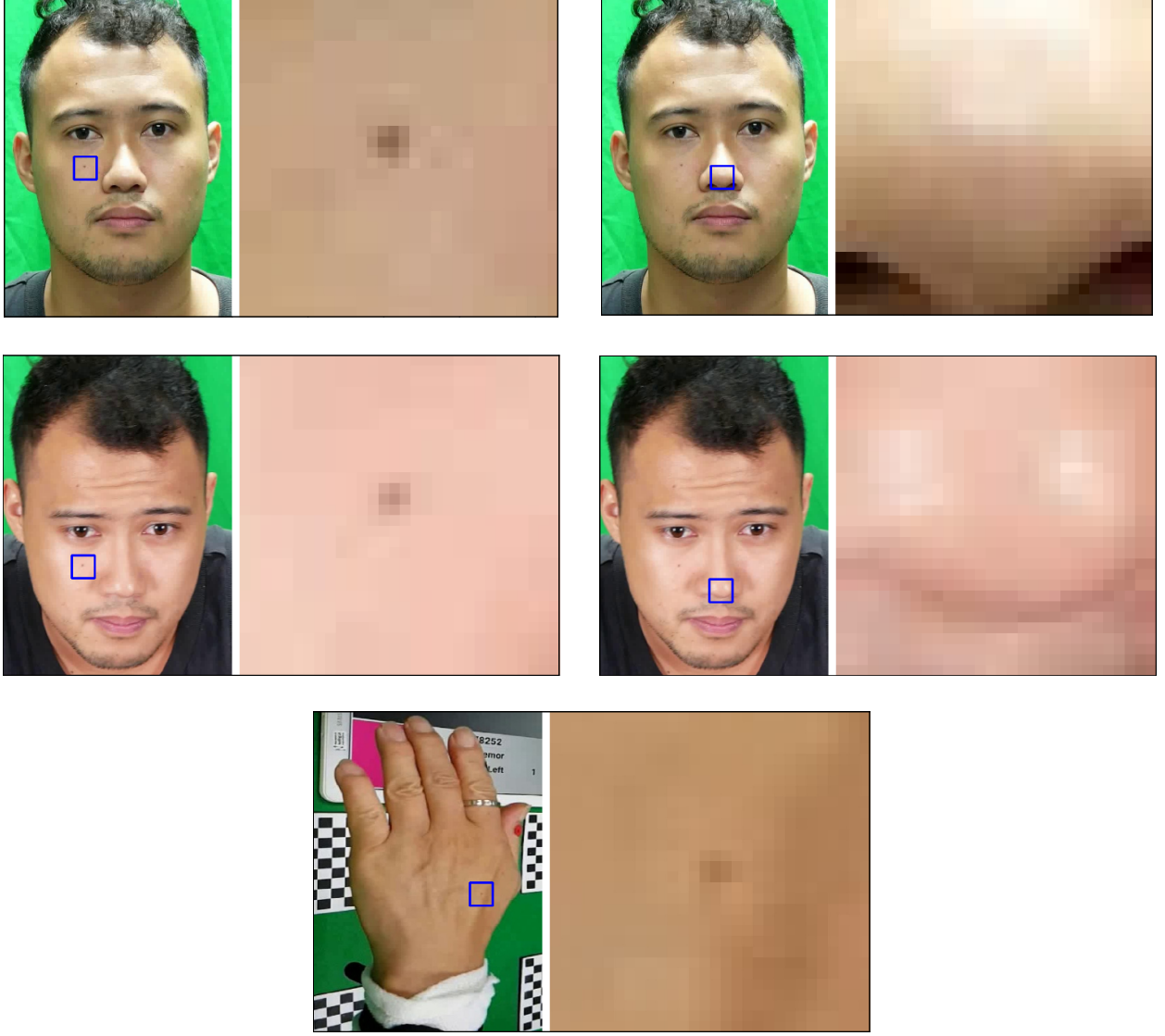


Figure 2: Reference crops of the face mole for static conditions (top-left), nose tip for static conditions (top-right), face mole for bike conditions (middle-left), nose tip for bike conditions (middle-right), and the hand mole of the PD patient marked (bottom) by the blue square of size 31×31 pixels and their magnifications for representative frames with resolution 420×300 pixels.

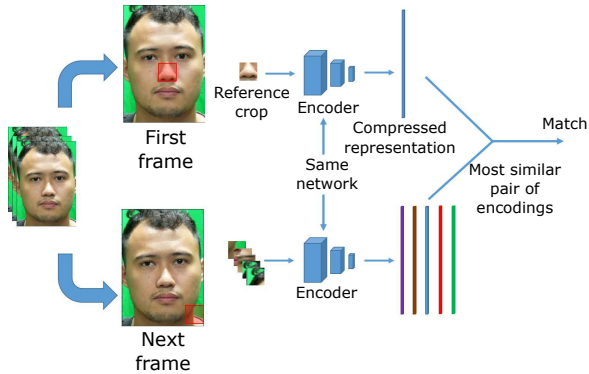


Figure 3: Flowchart of the algorithm for using an autoencoder for matching facial features.

for each image, body part, and motion condition. This yielded a distribution of the errors for the x and y coordinates that is normal, see section Normality tests for relabeling errors in x and y directions (Appendix A.4). Thus the sum of the stan-

Table 1: Standard deviations of the error distributions for the manual relabeling attempts.

	σ_x	σ_y
Static face mole	0.773	1.010
Static nose tip	1.165	1.256
Bike face mole	1.206	1.179
Bike nose tip	1.337	1.319
PD hand mole	1.162	0.915

dardized squared errors is Chi-square distributed. The standard deviations of δx and δy are different for each body part and motion condition, as shown in Table 1. The standard deviations of the errors for the nose tips are larger than for the moles. This is a result of the nose tip being a harder point to locate compared to a mole as it lacks the distinctive features necessary for a human to accurately pinpoint it from frame to frame. Thus we call the moles distinctive skin features.

To assess whether the errors are due to human mistakes in the relabeling or proper to the tracking method, we used the following metric. The test statistic, χ^2 , is the sum of the

standardized squared spatial errors

$$\hat{\chi}^2 = \sum_{i=1}^n \frac{\delta x(i)^2}{\sigma_x^2} + \frac{\delta y(i)^2}{\sigma_y^2},$$

where n is the number of frames and σ_x and σ_y are the standard deviations of the errors of the manual labelling for each condition (Table 1) for the x and y directions, respectively. We evaluated our test statistic on a Chi-square distribution with $2n$ degrees of freedom, $\chi^2(2n)$, to test our null hypothesis H_0 of the errors coming from human labelling. Note that significance values smaller than 5×10^{-324} can not be calculated in *numpy* and *math* packages in Python due to the finite precision of doubles.

2.5 Probability plot for Chi-square distributed errors

A Probability-Probability plot (P-P plot) is a graph of the percentiles of one distribution versus the percentiles of another (Holmgren, 1995). For two distributions with CDFs F_1 and F_2 the P-P plot can be represented in functional form as $F_1(F_2^{-1}(p))$ where p ranges between 0 and 1. It is used to determine how closely the distributions of two datasets agree. If two distributions are identical, then the values plotted in the P-P plot will lie on the $x = y$ line. Deviations from this straight line mean that one distribution stochastically dominates the other.

We plot the standardized squared spatial errors

$$e_{std} = \frac{\delta x^2}{\sigma_x^2} + \frac{\delta y^2}{\sigma_y^2}$$

of DFE against a Chi-square distribution with 2 degrees of freedom in Figure 9. The errors were standardized by the variances in Table 1.

2.6 Optical flow using Lucas-Kanade method

LK (Lucas and Kanade, 1981) uses spatial intensity gradients to direct the search for the best match. It is still a widely used method for sparse optical flow given that it is computationally fast and efficient, making it suitable for many real-time applications. It is assumed that the points in both images are in the same neighborhood and therefore have approximate registration, the brightness is relatively constant, and that distortions are linear.

For a small $m \times m$ window centered at point, p the local image flow velocity vector v must satisfy

$$\nabla I(q_i) \cdot v = -I_t(q_i),$$

where $I_t(q_i)$ and $\nabla I(q_i)$ are the temporal and spatial gradients respectively for each pixel q_i inside the $m \times m$ window. Assuming the window contains n pixels, denoted q_1, q_2, \dots, q_n , we can then write the equation on matrix form

$$\nabla I v = -I_t.$$

Here, the flow vector v represents the original position of the point of interest, denoted $p = [p_x, p_y]$ plus the image velocity vector $d = [d_x, d_y]$ at p , such that

$$v = \begin{bmatrix} v_x \\ v_y \end{bmatrix} = \begin{bmatrix} p_x + d_x \\ p_y + d_y \end{bmatrix}.$$

To deal with cases where the motion is large, *i.e.* more than one pixel, a typical approach is to apply LK on a pyramid of reduced-resolution images (Bouquet, 2001). The idea is to successively double the length of a pixel by halving the resolution and reducing fine image details that act as noise for large motion. A pyramid of images has its raw image I^0 as the lowest level of the pyramid and every subsequent image I^1, I^2, \dots, I^{L_m} being the image from the level below sub-sampled to be half the width and height. For the overall pyramidal tracking the algorithm first calculates the optical flow at the deepest level

of the pyramid L_m with the lowest resolution and uses that result as an initial guess for the next level L_{m-1} , the optical flow at this level is then used at L_{m-2} , and so on until level 0 (the original image). In our experiments, we used the implementation from OpenCV 3.4.2.17 with a pyramid of 5 levels, $L_m = 4$, with a 10×10 observation window at each level.

2.7 Feature matching using SIFT

SIFT (Lowe, 2004) is a method to create feature descriptors that are invariant to scale and rotation and enable robust feature matching across changes in viewpoint and illumination in the presence of noise and affine distortions. The idea is that the same keypoint in two images taken from, *e.g.*, different angles should have the same local information, *i.e.* gradients. The SIFT algorithm for extracting and describing distinctive invariant features, *i.e.* keypoints, can be divided into four parts: (i) construction of the scale space, (ii) keypoint localisation, (iii) orientation assignment, and (iv) generation of the keypoint descriptor. The keypoint descriptor of an image feature of interest is then compared to a database of keypoint descriptors for a second image to find the location of the same feature in it. We next describe the four parts, excluding some algorithm details, to foster understanding.

The scale space is constructed by repeatedly halving the image size and blurring at multiple different scales. To each image Gaussian blur is added to remove fine details and noise through convolution of the image with Gaussians, $G(x, y, \sigma)$, with different scales σ . This is implicit in the Difference of Gaussian (DOG)

$$D(x, y, \sigma) = (G(x, y, k\sigma) - G(x, y, \sigma)) * I(x, y),$$

separated by a scaling factor k , which is used to find blobs. The DOG pyramid is constructed one octave at a time by repeatedly taking every second pixel in each row and column of the previous image and calculating DOGs at different scales.

Keypoint localisation is based on finding the local scale space extrema in the constructed DOG pyramid of images and removing low contrast ones. Every extremum in its neighborhood of 26 surrounding pixels in the stack of images with different scales in each octave is considered a candidate keypoint. These are rather poorly localized in spatial and scale space. To obtain the location with subpixel accuracy and filter out low contrast keypoints, a second-order Taylor expansion of $D(x, y, \sigma)$ is computed at the extremum point, $z_0 = (x_0, y_0, \sigma_0)$, by approximating the derivative and Hessian using differences of neighbouring sample points

$$D(z_0 + z) = D(z_0) + D_z(z_0)^T z + 0.5 z^T D_{zz}(z_0) z.$$

The location of the extremum, \hat{z} is determined by taking the derivative and setting it to zero. The value of the DOG at this localized extremum is

$$D(\hat{x}, \hat{y}, \hat{\sigma}) = D(z_0 + \hat{z}) = D(z_0) + 0.5 D_{zz}(z_0)^T \hat{z}.$$

Keypoint candidates with $|D(\hat{x}, \hat{y}, \hat{\sigma})|$ less than a contrast threshold and poorly localized keypoints along an edge are discarded. Edge keypoints have a large principal curvature along the edge but a small principal curvature in the perpendicular direction, *i.e.* large ratio of the eigenvalues of the Hessian which in the spatial space (x, y) is defined as,

$$H = \begin{bmatrix} D_{xx} & D_{xy} \\ D_{xy} & D_{yy} \end{bmatrix}.$$

Any keypoint with an eigenvalue ratio above the edge threshold is discarded.

An orientation is assigned to each keypoint so its descriptor can be made rotation invariant. Based on the scale of the localized keypoint, $\hat{\sigma}$, the Gaussian smoothed image $L(x, y) = G(x, y, \hat{\sigma}) * I(x, y)$ closest in scale is selected. Then the gradient magnitude $m(x, y)$ and orientation $\theta(x, y)$ are computed using pixel differences:

$$m(x, y) = \sqrt{(L(x+1, y) - L(x-1, y))^2 + (L(x, y+1) - L(x, y-1))^2}$$

$$\theta(x, y) = \frac{\tan^{-1}((L(x, y+1) - L(x, y-1)))}{(L(x+1, y) - L(x-1, y))}.$$

A 36-binned orientation histogram with 10 degrees bin range is created from these for sample points in a region around the keypoint. The peaks in the histogram represent the dominant direction of the local gradients. The gradient magnitudes of the histogram are weighted by a Gaussian-weighted circular window with a σ that is 1.5 times that of the scale of the keypoint. Thus, the height of the bins represents the weighted sum of the gradient magnitudes in that area. Peaks correspond to dominant directions and the highest one determines the keypoint orientation.

Finally, the keypoint descriptor is generated. For each keypoint, after the dominant orientation is found, its coordinates and gradient orientations are rotated relative to this orientation to achieve orientation invariance. The magnitudes and orientations are then smoothed using a 16×16 weighted Gaussian window. A new orientation histogram is then calculated from the orientations of the smoothed 4×4 subregions which contain the sum of the gradients and magnitudes within that space. The histogram divides the orientations into 8 bins and the height of each bin is the magnitude of that orientation. This gives us 4×4 different histograms, each with 8 bins. The resulting feature descriptor consists of these histograms concatenated into a $4 \times 4 \times 8 = 128$ feature space. The feature descriptor vector is then normalized to unit length to achieve illumination normalization. We used the default implementation of SIFT in OpenCV 3.4.2.17. The parameters used were `nfeatures = 0`, `nOctaveLayers = 3`, `contrastThreshold = 0.04`, `edgeThreshold = 10`, and $\sigma = 1.6$.

After obtaining the keypoint descriptors, SIFT matches a set of keypoints from one image to a set of keypoints in another image by comparing the L2 norm of their residuals. In the original publication, SIFT used the Best Bin First (Beis and Lowe, 1997) algorithm to find approximate nearest neighbors and speed up the matching process. This process does not always return the nearest neighbor. Since we are interested in the ability of the methods to produce feature descriptors, we decided to use the global minimum of the L2 norm of the residuals instead.

We evaluated SIFT under two conditions. First, forcing it to select the point minimising the SSR. Second, allowing it to filter out points with the nearest neighbor to second nearest neighbor distance ratio greater than 0.8 to remove false positive matches for the high-dimensional descriptors, as described in the original publication (Lowe, 2004). In the second case, for the frames where the distance between the nearest neighbors exceeded the threshold, SIFT failed to find a matching feature. We, therefore, assigned the largest possible error to such frames, *i.e.* the length of the diagonal of the image 516.14 pixels.

2.8 Feature matching using SURF

SURF (Bay et al., 2006) is an algorithm largely based on SIFT. The main goal was to produce a faster feature detector-descriptor by reducing the computation time through several techniques to approximate the solutions used in SIFT. In addition, it also uses by default a simpler, 64-dimensional feature descriptor as opposed to the 128-dimensional feature descriptor used in SIFT.

The main differences between SIFT and SURF are the following: SIFT used the Difference of Gaussians to approximate the Laplacian of Gaussians, SURF pushes the approximation one step further and approximates it with box filters. Instead of the feature vectors representing the magnitude and orientation of the gradients, the feature descriptors of SURF are the sum of the Haar responses (and the absolute value of the responses) for the parallel x and normal y directions relative to the keypoint orientation. The Haar wavelet response is obtained by comparing how similar image patches are with square filters. The keypoint orientation is defined by the longest vector (largest magnitude) of the sum of Haar wavelet responses in a 2D plane which is defined by the horizontal response in the abscissa and the vertical response in the ordinate.

The extended version of SURF (named SURF-128) computes the sums of the Haar responses in the parallel direction

relative to the dominant keypoint orientation d_x and $|d_x|$ separately for the Haar responses in the normal direction relative to the dominant keypoint orientation $d_y \geq 0$ and $d_y < 0$. Similarly, the sums of d_y and $|d_y|$ are computed separately for $d_x \geq 0$ and $d_x < 0$. This yields a descriptor vector v for each of the 4×4 regions that is 8 dimensional, as opposed to the original 4 dimensional vector. Consequently, the length of the concatenated descriptors is doubled to 128 dimensions. We have used the extended version of SURF as implemented in OpenCV 3.4.2.17. The parameter values are `hessianThreshold = 100`, `nOctaves = 4`, `nOctaveLayers = 3`, `extended = true`, and `upright = false`.

2.9 Deep feature encodings

DFE aims to use unsupervised deep learning to learn skin feature representations that are better to track. We use an autoencoder that consists of an encoder subnetwork and a decoder subnetwork. The encoding subnetwork compresses the original data into a latent space that has typically fewer dimensions than the original input while the decoding subnetwork reconstructs the input from the compressed representation created by the encoder. Formally, we can describe the network as a composition of an encoder function f that creates a representation h of our input data x , and a decoder function g that reconstructs the input from the encoded data. We define the output reconstruction y in terms of the input x as

$$y(x) = g(f(x)).$$

Both f and g are functions constructed using 2D convolutional (LeCun et al., 2010) and transpose convolutional (Zeiler et al., 2010) layers. We used these as networks that have shown superhuman level performance for vision tasks all have this technology as their foundation (Bochkovskiy et al., 2020; Ren et al., 2015; Liu et al., 2016; He et al., 2017b; Szegedy et al., 2015; He et al., 2016). For our skin feature tracking application, these encoded representations h are the skin feature descriptors of image crops x that we compare to find matches of keypoints between face images.

For our experiments, we want to constrain the autoencoder to have a latent space of 128 features to make it a fair comparison with SIFT and SURF with rich descriptors. This architecture yields a compression factor of 0.0444 compared to the original input crop of size $31 \times 31 \times 3$. The loss function used to train the autoencoder was the Mean Squared Error (MSE) between input x encoded in the CIELAB space and its reconstructed output y which is also encoded in the same color space.

To encode the $31 \times 31 \times 3$ image crops into a 128-dimensional vector we use a symmetrical convolutional autoencoder architecture, see Figure 4. We downsample the spatial dimensions of the inputs by applying valid convolution operations and iteratively increase the number of channels by increasing the number of filters in our layers. To avoid overfitting and improve generalization, we apply Batch Normalization just before applying the activation function and right after the convolution operation. This allows the activation layer to receive unit Gaussian ($\mu = 0$ and $\sigma = 1$) inputs and for the network to control the diffusion of the outputs of the activation layer. In addition, Batch Normalization can become the identity function if the network deems that no normalization is needed. The non-linearity used at each hidden layer is the Rectified Linear Unit (ReLU), which constrains all the activations to non-negative values while preserving the magnitude of all positive inputs.

The network is symmetrical, so the decoder network is similar to the encoder network with the convolutional layers replaced by transposed convolutional layers to upsample the spatial dimensions of the input. The last transposed convolutional layer only has three filters so that the shape of the output is identical to the input and the loss function can be calculated from the feature map-channel pairs. The activation function in the last layer of the network is a Sigmoid to constrain the output values between 0 and 1. The optimizer Adamax is used, *i.e.* a variant of Adaptive Moment estimation (Adam) (Kingma and Ba, 2014). This network architecture contains 1,160,847

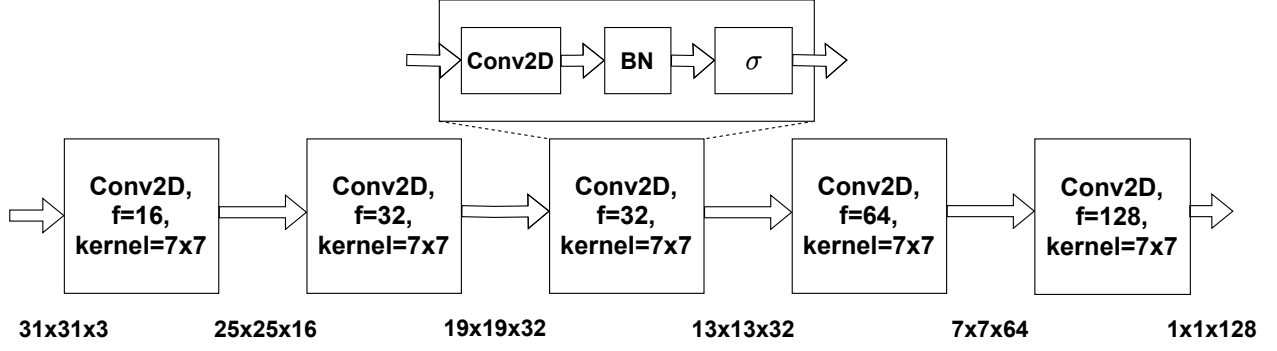


Figure 4: Encoder architecture of the autoencoder used in our experiments. The convolutional blocks are composed of three sequential operations: two-dimensional convolution (Conv2D), batch normalization (BN), and activation (σ). All convolutional layers are valid convolutions so the operation reduces the spatial dimensions of the input. The number of filters (f) and kernel size (kernel) in each block is given.

trainable parameters. It took approximately 138.9 hours to train it for 1000 epochs to a training MSE of 9.4×10^{-5} on our hardware.

2.10 Subpixel level prediction

By default LK estimate the location with subpixel level accuracy. Since we select the pixel whose feature descriptor minimizes the SSR with the reference descriptor, SIFT, SURF, and our DFE method only achieve pixel-level accuracy. To do a fair comparison of the methods, a subpixel level accuracy of the prediction from SIFT, SURF, and our DFE methods is needed. We perform subpixel level prediction by fitting a surface to the SSR between the reference point and all points of the second image and interpolating locally within a neighborhood of the pixel with minimum SSR (HajiRassouliha et al., 2018).

Let the SSR be represented as a function z , which is dependent on the x and y coordinates of points in the image, such that

$$z = f(x, y).$$

First, a pixel-level prediction is done by forcing the methods (SIFT, SURF, and DFE) to select the pixel with the minimum SSR through a global search for the minimum in the image space. Second, to obtain subpixel level accuracy a surface of order 2 is fitted to a 3×3 neighborhood of points around the global minimum by solving for c in the equation

$$z = Ac,$$

where $A = [1, x, y, xy, x^2, y^2]$ and z contains the SSR of the nine points in the 3×3 window. To prevent the matrix A from becoming ill-conditioned, we center the image coordinates around the 3×3 window by subtracting the coordinates of the middle pixel from all the pixels in the observation window. The surface equation is given by

$$z = c_6y^2 + c_5x^2 + c_4xy + c_3y + c_2x + c_1.$$

It is possible that for a single image there are multiple points with the same minimum SSR. In this case, we will select the point with the maximum curvature with a positive 2nd derivative z_{xx} . This ensures that our prediction is a local minimum. The curvature D is

$$D = z_{xx}z_{yy} - z_{xy}^2.$$

This is identical to finding the determinant of a 2×2 Hessian matrix

$$Hz(x, y) = \begin{bmatrix} z_{xx} & z_{xy} \\ z_{xy} & z_{yy} \end{bmatrix}.$$

If $D > 0$ and $z_{xx} > 0$, then according to Sylvester's criterion the Hessian $Hz(x, y)$ is positive definite and the surface has a local minimum. Similarly, if $D > 0$ and $z_{xx} < 0$, then the surface has a local maximum. If $D < 0$, then the eigenvalues

of $Hz(x, y)$ are of opposite sign, meaning the surface has a saddle point. If $D = 0$, then at least one of the eigenvalues of $Hz(x, y)$ is zero, yielding the test inconclusive (Abramowitz and Stegun, 1988; Thomas and Finney, 1961). That means that there is no curvature in at least one direction, *i.e.* L-shaped curve or flat surface. Any point that is not a local minimum will be discarded. Also Lowe discard a point if it does not meet the curvature criterion (Lowe, 2004).

Once the point with the lowest SSR, $D > 0$, and $z_{xx} > 0$ is found, the local minimum of z is the point where the gradients are zero in both directions, *i.e.* $z_x = 0$ and $z_y = 0$. We find this theoretical minimum of the surface by solving $\nabla f(x, y) = 0$, which yields

$$x = \frac{c_3c_4 - 2c_2c_6}{4c_5c_6 - c_4^2}$$

$$y = \frac{c_2c_4 - 2c_3c_5}{4c_5c_6 - c_4^2}.$$

2.11 Tracking

We evaluate the tracking of features using two extreme cases. The first uses only the information from the first frame, *i.e.* no update of the reference feature. A divergent error is less common in this tracking scheme as the method is always searching for the same reference feature in all frames. Even if the method matches the feature poorly, the error can be corrected due to the reference feature always remaining constant, but it is sensitive to change in the feature with time. This tracking scheme is just repeated feature matching frame by frame.

The second is using only the information from the previous frame, allowing the algorithm to replace the reference feature. This makes the tracking insensitive to gradual change in the feature with time. The reference feature is the representation in the 128-dimensional space of the point we want to locate from the previous frame. A divergent error is common as locating and associating features across many frames yields errors that can propagate when the method matches the feature poorly. For the case where we evaluate SIFT by its nearest neighbor to nearest neighbor ratio, we track the last prediction for which the ratio was less than the threshold even if it was several frames ago. That is to prevent SIFT from completely deviating. If SIFT can not assign a prediction, we assign the squared maximum possible distance to that image.

The errors are squared and standardized by the variances in x and y directions of each body part and motion condition. These are presented in a cumulative sum for each frame. A 99% CI line is plotted by evaluating the inverse of the χ^2 CDF evaluated at a probability of 0.99 with $2n_{\text{frame}}$ degrees of freedom, where n_{frame} is the frame number.

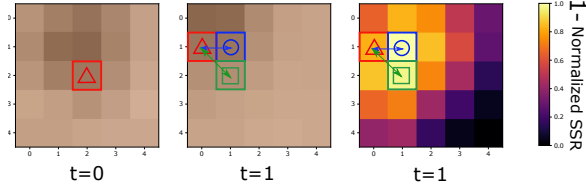


Figure 5: Descriptor distance and spatial distance of nearest neighbors. The nearest neighbor (marked by blue circle) is the point with minimum SSR compared to the reference feature. By extension, the second nearest neighbor (marked by green square) is the point with the second-lowest SSR. In this case, the spatial distances to the ground truth (marked by red triangle) of the nearest and second nearest neighbor (marked by the blue and green arrows) are 1 and 1.44 pixels, respectively. The left image shows a 5×5 enlargement of the hand mole on the original image, the middle image shows the same feature in a second image with a displacement of 2 pixels to the left and 1 pixel up, the right image shows the SSR values of the displaced image.

2.12 Analysis of feature matching

The aim of feature matching is to find the location of the feature of interest in another image based on similarity of the feature descriptors, which we measure using the sum of squared residuals. The point with the smallest descriptor distance, *i.e.* minimum SSR, is called the nearest neighbor. The point with the second smallest SSR, the second nearest neighbor and so forth. For feature matching to correctly locate the feature of interest the point with smallest descriptor distance should also have the smallest spatial distance to the true location of the feature of interest. The relation between the spatial and descriptor distance is illustrated for the hand mole in Figure 5. The spatial distance refers to the Euclidean distance, *i.e.* difference in position between two points in an image.

When calculating the distance between two high-dimensional vectors, certain variables contribute to the distance more than others. SIFT employed a check for the nearest neighbor to second nearest neighbor ratio to avoid the high number of false positives that arise due to this phenomenon. We investigated the ratio of the nearest neighbor to the second nearest neighbor based on the descriptor distance to the reference point for our DFE method (Appendix A.11).

3 Results

3.1 Feature matching accuracy

Deep feature encoding alone located the skin features in every frame. It also had the smallest mean error in all cases except the static nose tip, see Table 2. For the static nose tip case, its performance is still comparable to SIFT and LK, with the latter being the best method in terms of the mean error. SIFT with threshold and SURF did not perform well under any body part-motion combination. The matching of all methods was made with sub-pixel level accuracy. The frame count for the static, bike, and PD conditions was 260, 169, and 39 frames; respectively. It is worth noting that the maximum possible distance in all cases is 516.14 pixels, equaling the length of the diagonal of the images of size 420×300 pixels.

The distance errors (in pixels) of all methods sorted in descending order for each body part and motion condition is shown in Figure 6. We note that LK is comparable to DFE for the static conditions. The best performance for SIFT was while tracking the nose tip under static conditions. SURF and SIFT with the recommended nearest neighbor to second nearest neighbor threshold did not perform well in any of the scenarios we tested. Our Deep feature encodings method was the

only method to perform well in every condition. Even while tracking the nose tip under bike conditions the error was at most 6.5 pixels. For the distinctive features, *i.e.* moles, the error was at most 2.1 pixels, while it exceeded 219 for the other methods in some conditions.

3.2 Tracking

The results for tracking only the reference feature from the original image is shown in Figure 7 and replacing the reference feature with the prediction from the previous frame in Figure 8. The average errors using the reference feature from the original image are shown in Table 2 and replacing the reference feature with the prediction from the previous frame in Table 3. In general, DFE is clearly the best method for tracking, achieving the lowest mean error for all conditions except the nose tip under static conditions. In the former case, the cumulative sum of standardized squared errors of DFE even remain within the 99% confidence interval for the distinctive skin mole. In the latter case, it exceeds it, but all other methods have mean errors greater than 100 pixels. The large mean errors are due to the divergence problem discussed in section Materials and Methods. In this tracking scheme, LK also diverges in all conditions, while it in the former scheme did not for the static condition. This renders it not useful for tracking. In contrast, DFE remains useful as it did not diverge; even when all other methods did. The ratios of nearest to second nearest neighbors for SIFT with threshold consistently exceeded the 0.8 as time increased. This is a result of the method diverging to the point where it is no longer tracking features that are distinctive enough for it.

3.3 Probability plot for Chi-square distributed errors

For tracking the moles the empirical data falls on or below the $x = y$ line of the P-P plot in Figure 9 and 11, while it for the nose tip falls above the $x = y$ line. This means that for the face mole, the errors of DFE are likely due to human labelling. On the other hand, the errors for the nose tips are likely in part due to the method; as is the case for all other methods, see Table 4. This further emphasizes our assumption that the mole is a more distinctive feature that is easier to track.

The significance level at which we can reject the null hypothesis of the errors coming from human labelling for all conditions, previously described in section Chi-square analysis, can be seen in Table 4. This hypothesis cannot be rejected for DFE when tracking the moles, nor for LK when tracking the face mole under static condition. The χ^2 -test statistic is so small that the significance level is near one for DFE. The significance level of SURF for all conditions was smaller than the minimum precision of doubles of 5.0×10^{-324} .

3.4 SSR as a function of spatial coordinates

We looked into the extreme cases for localization performance of SIFT, SURF, and DFE methods. Figure 10 shows the SSR landscape of the frame with the smallest localization error for tracking the face mole under bike conditions. We chose this condition because for the best cases the localization error of all methods is below one pixel of distance. We can see that the SSR landscape of SIFT and SURF is chaotic and does not have any clear structure or pattern. This is in contrast to the SSR landscape of our DFE method which has smaller values near the face. This observation holds independent of the methods localization performance (Appendix A.13). This suggests that our method is better at creating feature descriptors for skin features than the other state-of-the-art methods. A structured SSR landscape will prevent the algorithm from selecting a false positive which is spatially far from the ground truth.

Table 2: Mean errors (in pixels) for feature matching using the same reference feature. The best results are highlighted in bold. SIFT* stands for SIFT with the nearest neighbors threshold.

	SIFT	SIFT*	SURF	LK	DFE
Static face mole	17.28	230.09	93.84	1.08	1.04
Static nose tip	2.37	385.69	48.13	2.16	2.47
Bike face mole	16.33	216.25	74.93	4.68	0.90
Bike nose tip	64.12	421.99	116.63	11.31	3.31
PD hand mole	17.29	227.19	85.27	33.67	0.64

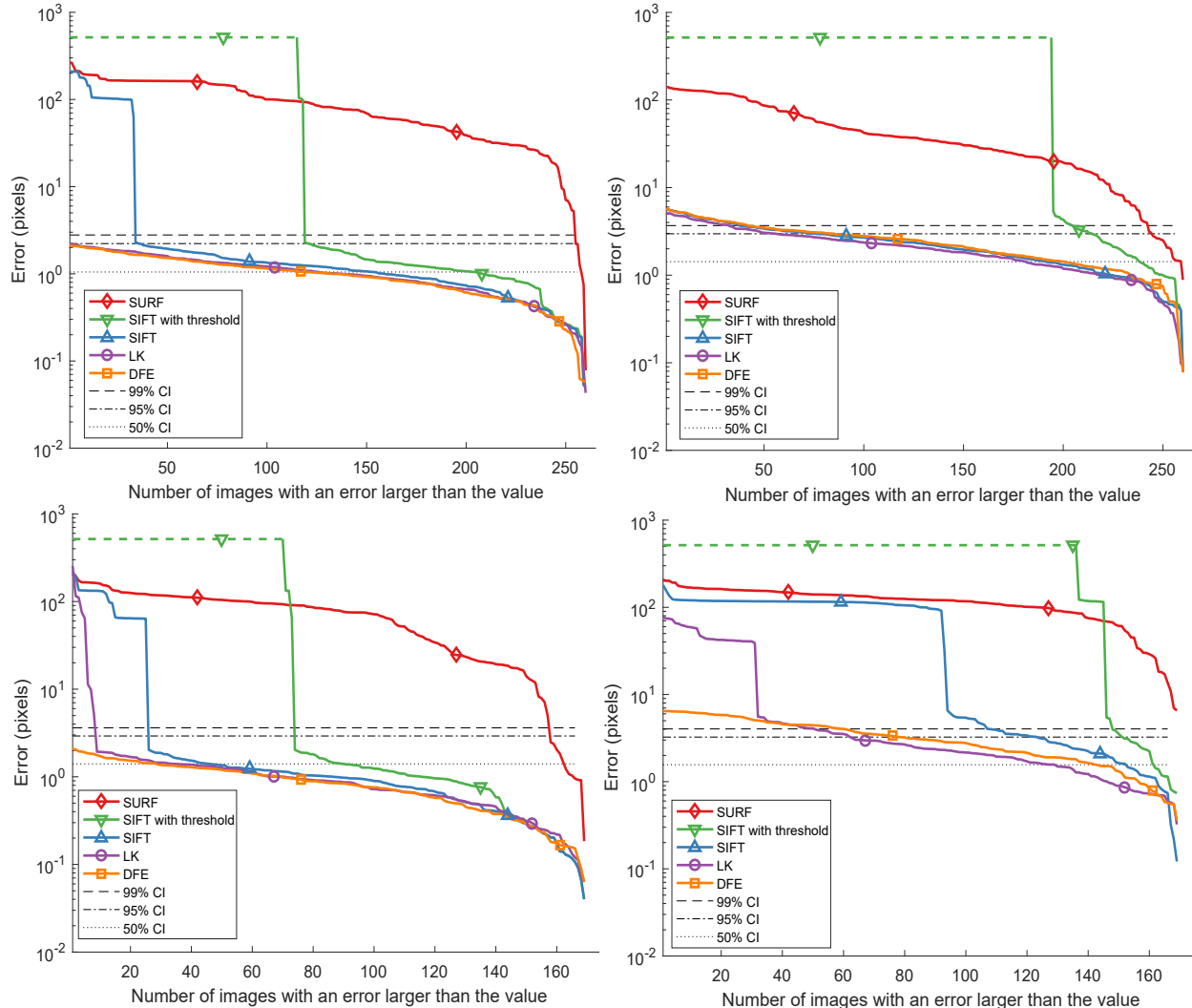


Figure 6: Sorted errors for matching the face mole under static conditions (top-left), nose tip under static conditions (top-right), face mole under bike conditions (bottom-left), and nose tip under bike conditions (bottom-right). The black lines represent the 50%, 95%, and 99% CI from the simulated Chi-square distribution. The green dashed line for SIFT with threshold stands for the frames where the nearest neighbor distance threshold was larger than 0.8.

Table 3: Mean errors (in pixels) for tracking using the prediction of the previous image as a reference feature. The best results are highlighted in bold. SIFT* stands for SIFT with the nearest neighbors threshold.

	SIFT	SIFT*	SURF	LK	DFE
Static face mole	191.81	514.16	178.66	179.99	2.15
Static nose tip	70.62	514.16	173.83	135.94	4.24
Bike face mole	144.41	513.09	149.95	293.76	2.56
Bike nose tip	142.41	513.09	150.49	244.70	2.30
PD hand mole	142.22	502.92	150.16	162.07	1.30

3.5 Generalisation to PD data

The performance of the methods is qualitatively the same as for the face mole under bike conditions based on a comparison of Figures 11, 6, 7, 8, and 9. DFE is still the best method for

tracking the mole on the hand of the PD patient. In contrast to Figure 6, the second-best method is SIFT, followed by LK. Although the images in this dataset are qualitatively similar and there is little distortion due to motion, both SIFT and LK for some images yield errors exceeding 100 pixels. This

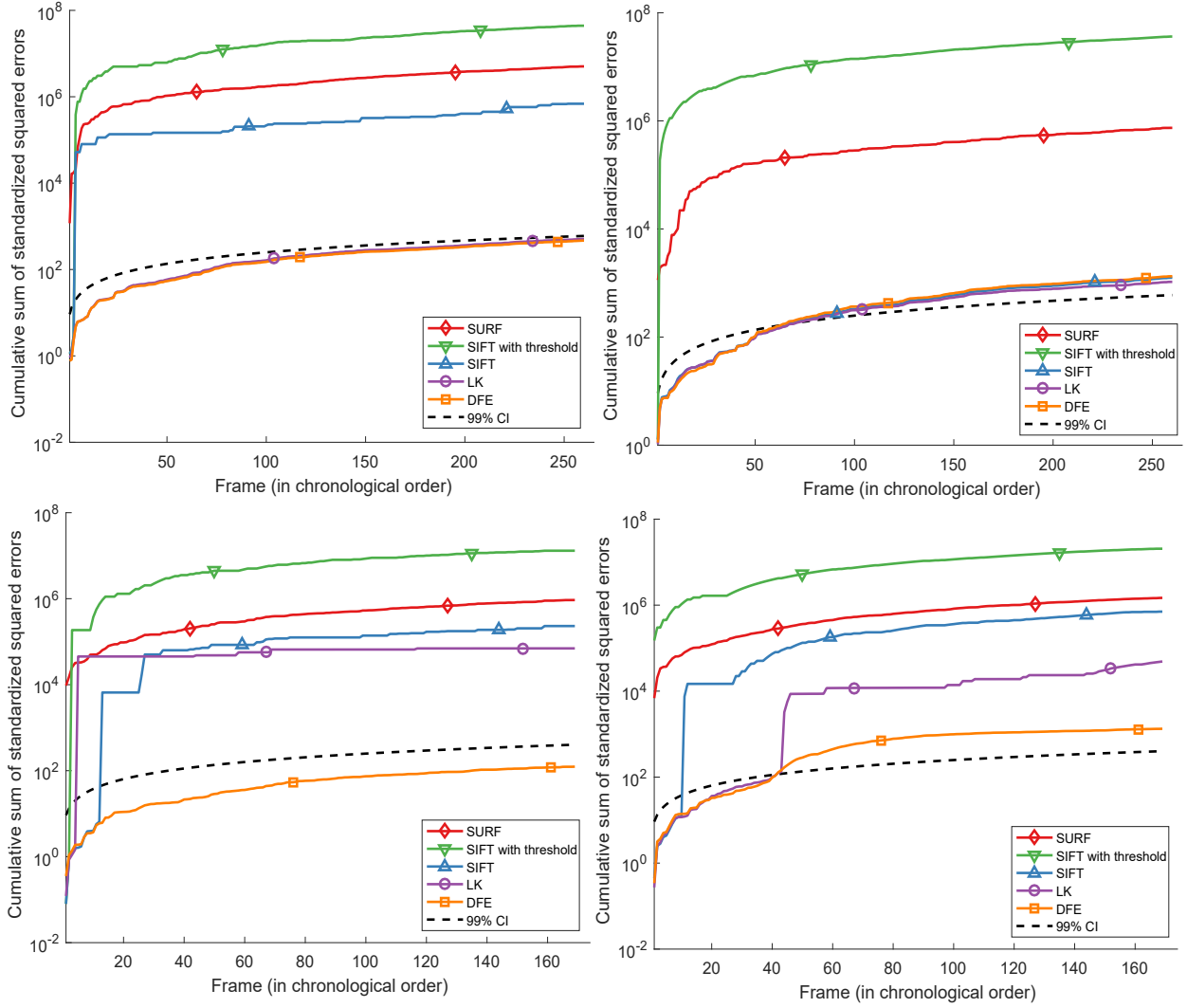


Figure 7: Cumulative sum of standardized squared errors using the reference feature from the original image for tracking the face mole under static conditions (top-left), nose tip under static conditions (top-right), face mole under bike conditions (bottom-left), and nose tip under bike conditions (bottom-right). The black dotted line marks the 99% CI line.

Table 4: Significance level at which the null hypothesis of the errors coming from human labelling is rejected. Values larger than 0.01, representing the threshold to reject the null hypothesis with 99% confidence, are highlighted in bold. ϵ stands for a value smaller than the smallest increment of doubles, *i.e.* 5.0×10^{-324} .

	SIFT	SURF	LK	DFE
Static face mole	ϵ	ϵ	0.64	0.95
Static nose tip	2.6×10^{-62}	ϵ	3.7×10^{-38}	7.9×10^{-73}
Bike face mole	ϵ	ϵ	ϵ	1.0
Bike nose tip	ϵ	ϵ	ϵ	4.4×10^{-118}
PD hand mole	ϵ	ϵ	ϵ	1.0

makes the result qualitatively closer to the face mole under bike conditions than static conditions. SURF again failed to track the mole. For DFE the errors are likely due to human labelling and not the method itself since the sampled errors are lower than the $x = y$ line in the P-P plot. Figure 12 shows that the SSR landscape of DFE has more structure than the landscapes produced by either SIFT or SURF for the image with smallest error. The tracking results are also qualitatively similar to the ones shown in Figures 7 and 8. These show that DFE is the best tracking method, no matter what tracking scheme is employed, as it was the only method that did not diverge. It also shows that usage of the reference feature from the original image resulted in a smaller cumulative error. These results are qualitatively similar to Figures 7 and 8.

4 Discussion and Conclusions

We present an algorithm that is more accurate and precise, and more importantly, reliable for skin feature matching than the traditional Computer vision methods under the conditions of interest for our ballistocardiography and Parkinson’s disease applications. It is more precise thanks to the global minima containing several nearest neighbors within the range of acceptable predictions without the inherent problem of a large number of false positives that arise from calculating the similarity of two high-dimensional feature vectors in SIFT and SURF. The distinctiveness of the feature representations can be attributed to three main factors: preservation of spatial information through the convolution operation, learning of complex features through hierarchical feature learning, and the

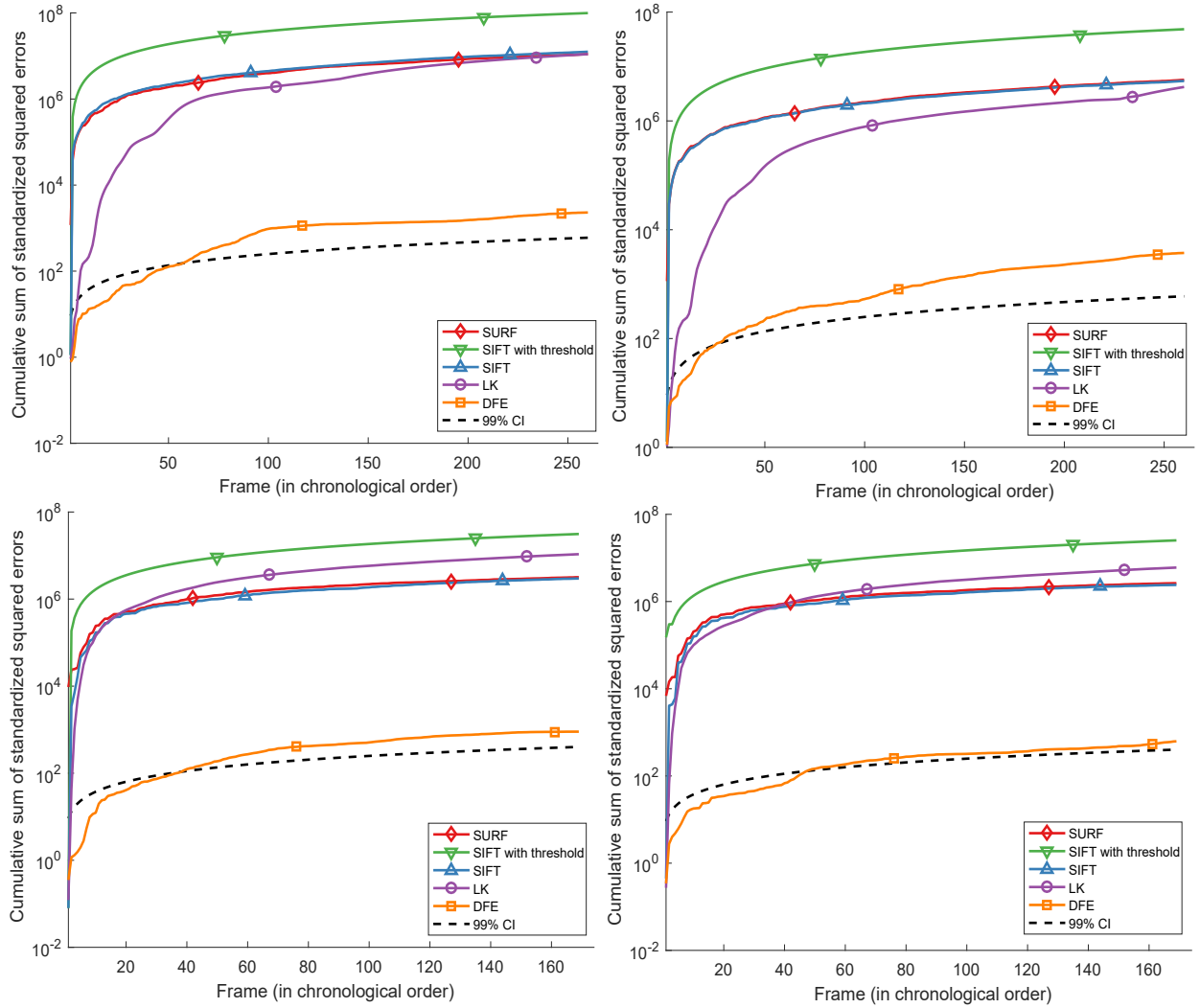


Figure 8: Cumulative sum of standardized squared errors using the prediction from the previous image as reference feature for tracking the face mole under static conditions (top-left), nose tip under static conditions (top-right), face mole under bike conditions (bottom-left), and nose tip under bike conditions (bottom-right). The black dotted line marks the 99% CI line.

creation of a set of latent variables that is able to capture the variance of the samples. As demonstrated in our experiments, when the matching method makes an obviously wrong prediction of the location of the skin feature, the error is usually extremely large. This will cause tracking algorithms to diverge.

To ensure that our testing is exhaustive, yet simple, and that large changes cannot cause trouble, we currently do not search locally for features but rather do a global search for the best match. Thus, our method is not computationally optimized. It currently takes approximately four times longer than SIFT to run on the validation data with our hardware. We could assume that the skin features have approximate registration and perform a local search to speed up the computation in the future. In addition, the matching scheme could be sped up by implementing an approximate technique for matching neighbors as it has been demonstrated in SIFT. The search could also be optimized if we took advantage of the convexity of the search space, which we have locally for DFE in all cases. We have not considered the occlusion of the key point.

In conclusion, there is still much work to be done before our pipeline is useful in the vast majority of situations. However, the Deep feature encodings have already shown promising results in terms of precision and accuracy for matching features in our applications. Previous feature tracking and feature matching methods are not good enough for the applications we are interested in.

5 Statements and declarations

5.1 Acknowledgments

We thank Chien-Chih Wang for collecting the ballistocardiography data as a part of this Master's thesis work.

5.2 Funding

This research was supported by the Ministry of Science and Technology in Taiwan (MOST 108-2218-E-006-046, 109-2224-E-006-003, and 110-2222-E-006-010).

5.3 Competing interests

The authors have no financial or non-financial interests that are directly or indirectly related to the work submitted for publication.

5.4 Ethics approval

The use of the UTKface and remote ballistocardiography datasets was reviewed and approved by the National Cheng Kung University Human Research Ethics Review Committee

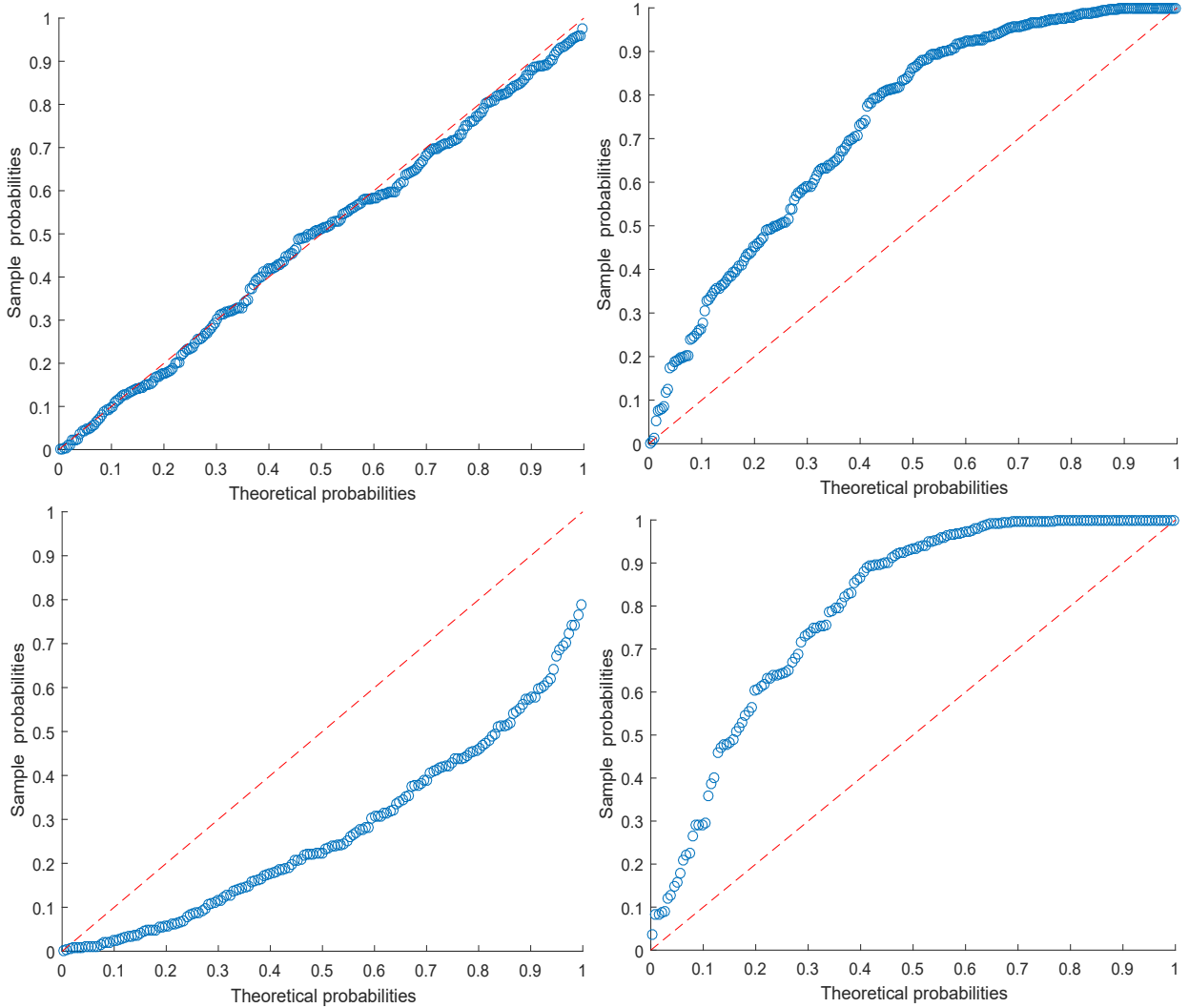


Figure 9: P-P plot for the standardized squared spatial errors for tracking the face mole under static conditions (top-left), nose tip under static conditions (top-right), face mole under bike conditions (bottom-left), and nose tip under bike conditions (bottom-right) for DFE. The red dashed line marks the $x = y$ line and deviations from this line represent deviations from the theoretical Chi-square distribution.

under case 108-244. The use of the Parkinson’s Disease postural tremor test dataset was reviewed and approved by the Kaohsiung Medical University Chung-Ho Memorial Hospital Institutional Review Board under the number KMHIRB-E(I)-20190173.

5.5 Data

Our ethics approval does not allow us to make the validation data publicly available. The training of the autoencoder used in the Deep Feature Encodings can be reproduced using the publicly available UTKface dataset.

5.6 Code availability

Our method can be easily implemented based on the description in the article and pseudo code in the Appendix A.7.

5.7 Authors’ contribution

Author contribution using the CRediT taxonomy: Conceptualization: TN; Data curation: JC; Formal analysis: JC; Methodology: JC and TN; Investigation: JC; Software: JC; Verification: JC and TN; Visualization: JC and TN; Writing

- original draft preparation: JC; Writing - review and editing: TN; Funding acquisition: TN; Project administration: TN; Resources: TN; Supervision: TN.

A Appendix

A.1 Autoencoders for feature construction

An autoencoder is a type of neural network that uses an unsupervised training strategy to learn the identity function, see Figure 13. As such, it can be trained by minimizing the discrepancy or distance between the original input data and its reconstruction. The identity function may seem like a trivial and meaningless function to learn. However, if we constrain the latent space to have fewer dimensions than our input, then we force the network to learn the most salient and distinctive features of our data.

Their use for dimensionality reduction was popularized in 2006 by Geoffrey Hinton (Hinton and Salakhutdinov, 2006). Similar to Principal Component Analysis, a key feature of autoencoders is their ability to encode the input data into latent state representations that provide insight into the samples of the data. Strictly speaking, an autoencoder only requires a

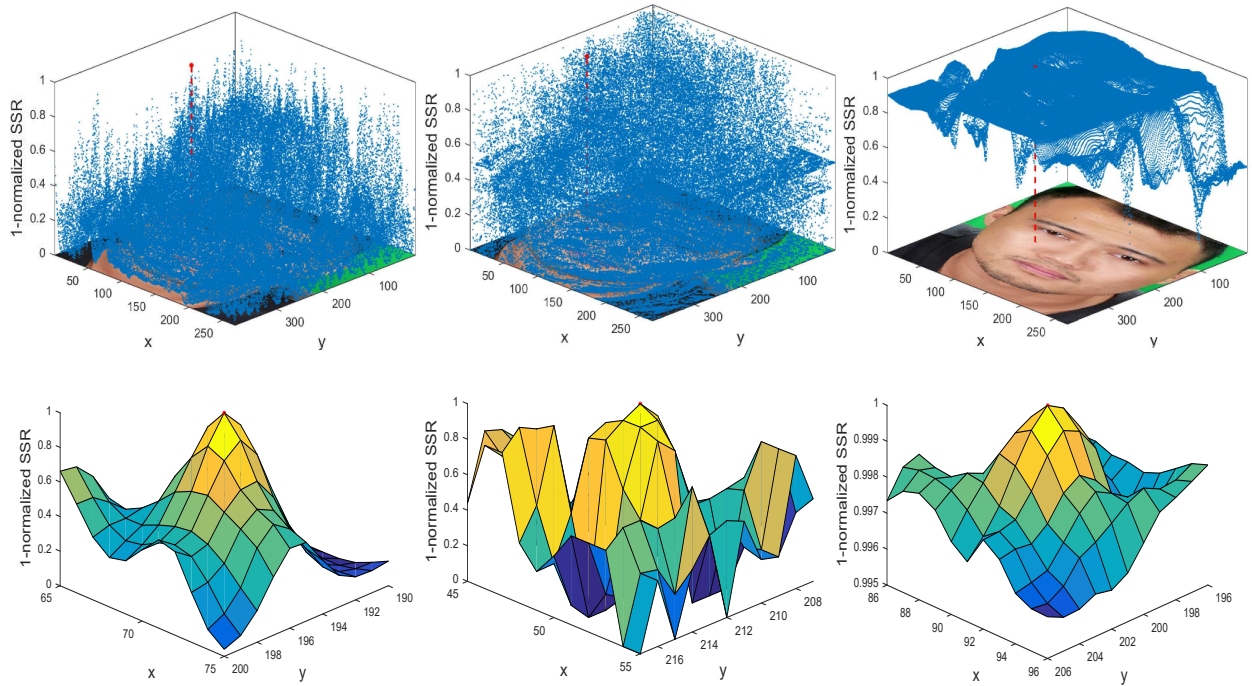


Figure 10: SSR as a function of the spatial image coordinates for the images with the smallest localization errors for tracking face moles under bike conditions for SIFT (left), SURF (middle), and DFE (right) and their corresponding regional enlargements of the optimum. The red dashed lines mark the point in the space with minimum SSR, which is plotted as a red circle. The distances to the ground truth are 0.04, 0.98, and 0.06 pixels, respectively.

single encoder and a single decoder layer. However, there are several advantages of adding depth to the architecture of these networks, *e.g.* fewer computations required to represent some functions, fewer data needed to learn some functions (Goodfellow et al., 2016), better compression compared to their shallow or linear counterparts (Hinton and Salakhutdinov, 2006).

Convolutional Auto Encoders (CAE), sometimes also referred to as Stacked Convolutional Auto Encoders, are a type of deep autoencoder that uses regional information to reconstruct inputs that are two- or three- dimensional. In a standard autoencoder, the layers in the encoder and decoder are fully connected. A CAE maintains the same structure as the standard autoencoder but replaces the fully-connected layers with convolutional layers when downsampling and transpose convolutional layers when upsampling (Dumoulin and Visin, 2018). Similarly, as the standard autoencoder, the CAE also learns abstractions from the data even when the CAE is complete, *i.e.* when the dimensionality of the latent space is as large as the input (Manakov et al., 2019).

Due to their ability to consider spatial information, CAEs have been especially useful when analyzing imaging data. A deep CAE was used to cluster the embedded features of imaging data of several benchmark datasets (Guo et al., 2017). The method, coined Deep Convolutional Embedded Clustering, can create features that were used to cluster the MNIST handwritten digits with an accuracy of 0.8897. Some other CAE applications include removing artifacts in images, denoising images, and coloring grayscale images. Here we use a CAE to learn skin features.

A.2 Statistics of the training dataset

UTKface dataset of faces in the wild contains 24,108 faces gathered from the internet. The face images are labeled by age, gender, and ethnicity; see Figure 14. The ground truth of age, gender, and race are estimated through the Deep EXpectation (DEX) algorithm (Rothe et al., 2018) and verified by a human annotator. Each image was cropped to ensure the face dominates it. The face was in each image detected using the

OpenCV-ResNet-10 based model. The areas of the cropped faces are shown in Figure 15.

A.3 CIELAB color space

All the images in the UTKface dataset are coded using the RGB color model. This color model is the conventional model in which most images are created or displayed. However, this color model is device-dependent, *i.e.* given that the images were created using cameras with different white points (reference whites, target whites) the colors would be represented differently. In addition, the RGB color model does not accurately represent how humans see color. A large sum of squares differences in a pair of crops might not make them seem very different to our eyes, *e.g.* we consider light green to be similar to yellow but not to red and we consider yellow to be very different from black but more similar to white. Since we want to train a device independent autoencoder to reconstruct image crops, we are interested in a reconstruction that is device independent and minimizes differences in accordance with how our visual system perceives them.

In 1976 the International Commission on Illumination (Commission internationale de l’éclairage in French, CIE) defined the CIELAB color space (also known as CIE $L^*a^*b^*$). It is a device-independent color model that defines colors relative to the white point of the CIE XYZ space from which they were converted. It represents colors in three axes:

1. L^* for lightness: Ranging from 0 as black to 100 for white.
2. a^* for green-red color channels: Ranging from -127 for green to 127 to red.
3. b^* for blue-yellow color channels: Ranging from -127 for blue to 127 to yellow.

Here the asterisk (*) is pronounced star and is added in order to differentiate the L^* , a^* , and b^* from Hunter’s L , a , and b . The color gamut of CIELAB includes the gamut of the RGB color model, ensuring no information is ignored at the conversion see, Figure 16.

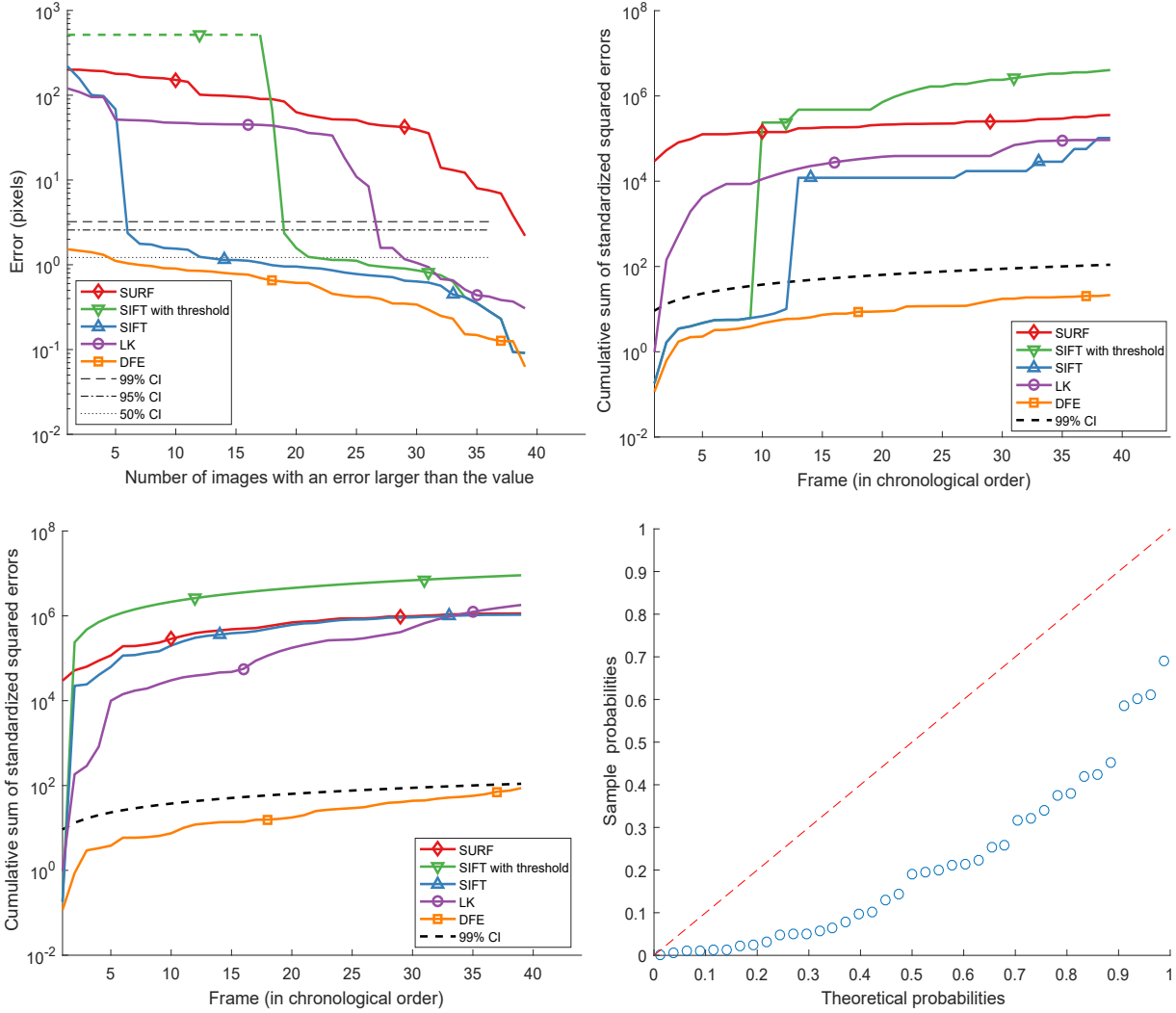


Figure 11: Results of running the methods for tracking the mole on the hand of the PD patient. Sorted errors for tracking the mole (top-left), cumulative error for tracking using the reference feature from the original image (top-right), cumulative error for tracking using the reference feature from the previous image (bottom-left), and P-P plot for the standardized squared spatial errors (bottom-right).

The CIELAB color space aims to be perceptually uniform, *i.e.* the nonlinear relations for L^* , a^* , and b^* are intended to mimic the nonlinear response of the eyes when looking at different colors. As such, the Euclidean distance between two colors is proportional to the color difference perceived by the standard (colorimetric) observer (Colantoni et al., 2016). In addition, unlike many color spaces that use cylindrical representations of the hues of colors (HSV, HSL, or HSB), the color representations are non-periodic. This property is especially good for training machine learning models that minimize the sum of squared residuals as the same hue of color can have drastically different values. In HSV the red hue ranges from roughly 345 to 15 with a transition to 0 at 360 in the H channel.

i.e. common sRGB, to CIELAB color space is given by:

$$\begin{bmatrix} X \\ Y \\ Z \end{bmatrix} = \begin{bmatrix} 0.412453 & 0.357580 & 0.180423 \\ 0.212671 & 0.715160 & 0.072169 \\ 0.019334 & 0.119193 & 0.950227 \end{bmatrix} \begin{bmatrix} R \\ G \\ B \end{bmatrix}$$

$$X = X/X_n, \quad \text{where } X_n = 0.950456$$

$$Z = Z/Z_n, \quad \text{where } Z_n = 1.088754$$

$$L = \begin{cases} 116 * Y^{1/3} - 16 & \text{for } Y > 0.008856 \\ 903.3 * Y & \text{for } Y \leq 0.008856 \end{cases}$$

$$a = 500(f(X) - f(Y))$$

$$b = 200(f(Y) - f(Z)),$$

where

$$f(t) = \begin{cases} t^{1/3} & \text{for } t > 0.008856 \\ 7.787t + 16/116 & \text{for } t \leq 0.008856. \end{cases}$$

CIELAB is copyright and license-free. It is also mathematically fully defined. A conversion of a floating point image (with intensity range of 0 to 1) in the RGB color space, with a reference white point given by the CIE standard illuminant D65,

The aforementioned conversion is the one employed in OpenCV under the assumption that the image uses the sRGB profile. The conversion takes as inputs floating point RGB (ranging 0 to 1) and outputs CIELAB values with ranges in L^* from 0 to 100, a^* from -127 to 127, and b^* from -127 to 127. It is typical when a variable has a defined upper and lower bound, to normalize it to values between 0 and 1. This will also allow us to directly compare the outputs of the prediction layer in the convolutional autoencoder which has a Sigmoidal function to constrain the values within this range. To normalize

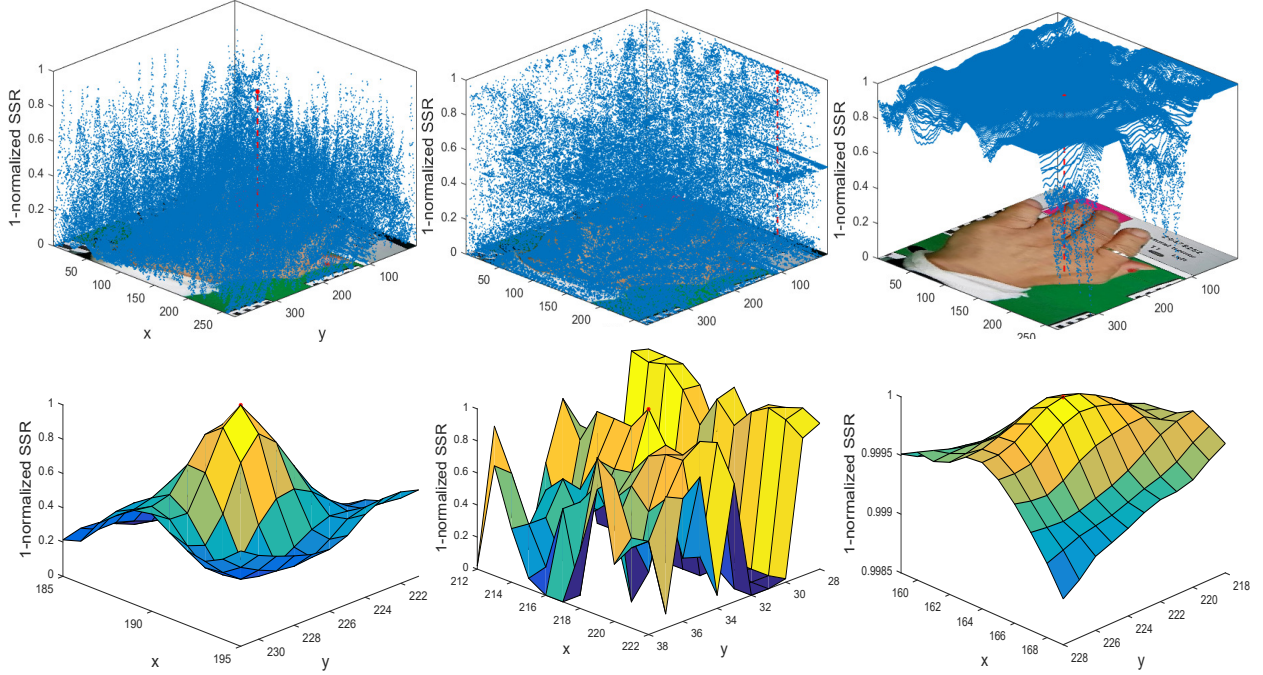


Figure 12: SSR as a function of the spatial image coordinates for the images with the smallest localization errors for tracking the mole on the hand of the PD patient for SIFT (left), SURF (middle), and DFE (right) and their corresponding regional enlargements of the optimum. The red dashed lines mark the point with minimum SSR. The distances to the ground truth are 0.09, 196.12, and 0.06 pixels, respectively.

each of these channels to the 0 to 1 range we have implemented a channel-wise min-max normalization technique.

$$x' = \frac{x - \min(x)}{\max(x) - \min(x)}.$$

Here $\min(x)$ and $\max(x)$ are the absolute minimum and maximum of each respective channel in the CIELAB color space.

Since the images in the UTKface dataset were obtained from the internet, it is not clear if they are encoded in standard RGB using white point D65 or not. However, we assumed all of these to be in standard RGB as this is considered to be the default color space for the internet (Anderson et al., 1996). The images collected for the remote ballistocardiography dataset were collected using a Panasonic GX85 camera with a default standard RGB color space. The images from the Parkinson’s disease postural tremor test were collected using the main camera of a Samsung S7 phone which also encodes them in standard RGB.

A.4 Normality tests for relabeling errors in x and y directions

The errors in both x and y directions were calculated by subtracting the mean of 6 relabeling attempts for each of the 15 images and concatenating them into a vector with 90 elements.

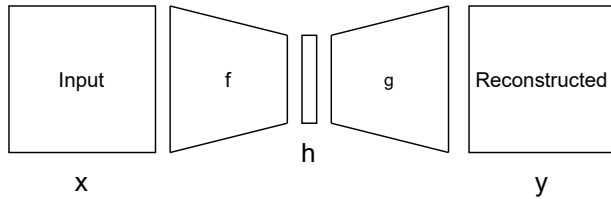


Figure 13: Typical architecture of an autoencoder network. The input x is compressed into a representation h through f ($h = f(x)$) and then a reconstruction y is created from h through g ($y = g(h) = g(f(x))$).

Table 5: Number of states that the relabelling errors in both x and y directions are quantized into (n_{quant}).

	n_{quant}		Range	
	δ_x	δ_y	δ_x	δ_y
Static face mole	19	21	4.5	5.5
Static nose tip	25	30	5.5	5.7
Bike face mole	31	26	6.0	5.5
Bike nose tip	31	28	6.3	6.0
PD hand mole	26	22	6.8	4.5

The labelling of the image was done at pixel level by a human operator repeatedly clicking on the screen to label the feature. Since the range of the relabelling errors is small, this yields data that is quantized into n_{quant} values which are shown in Table 5.

Quantization of a normal distribution makes the distribution more similar to a binomial distribution (Tarongi and Camps, 2010). Therefore, when applying normality tests, *e.g.* Lilliefors tests, the data looks non-normal. To avoid this, the number of quantization levels must increase as the sample size increases. The results of a Monte Carlo simulation of sampling 1000 standard normal distributions of 90 values each and applying the Lilliefors test for normality is shown in Figures 17. Only 90 values were drawn to match the number of relabeling errors. These were binned into 1 to 150 bins and replaced by the bin center after min max normalisation to 0 to 1. For the number of quantization states seen in our data (19-31) the Lilliefors test is misleading.

However, quantization only affects the CDF of a distribution by making it look less smooth and more like a staircase. We standardized the errors in x and y directions by their respective standard deviations and compared them against a theoretical standard normal distribution ($\mu = 0$ and $\sigma = 1$) in Figures 18, 19, and 20. Using this method, we can determine that the manual labelling errors are normally distributed.

Given that the errors in x and y directions are normal, the

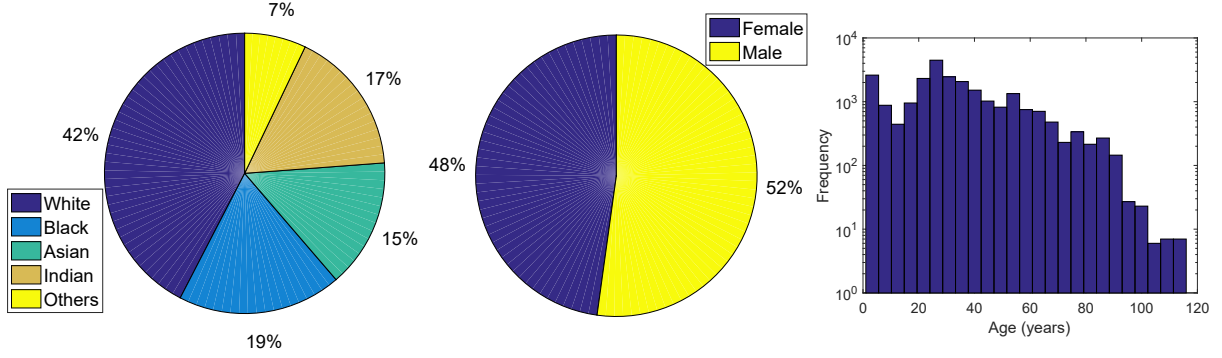


Figure 14: Demographic information of race (left), sex (middle), and age (right) of the UTKface wild faces dataset.

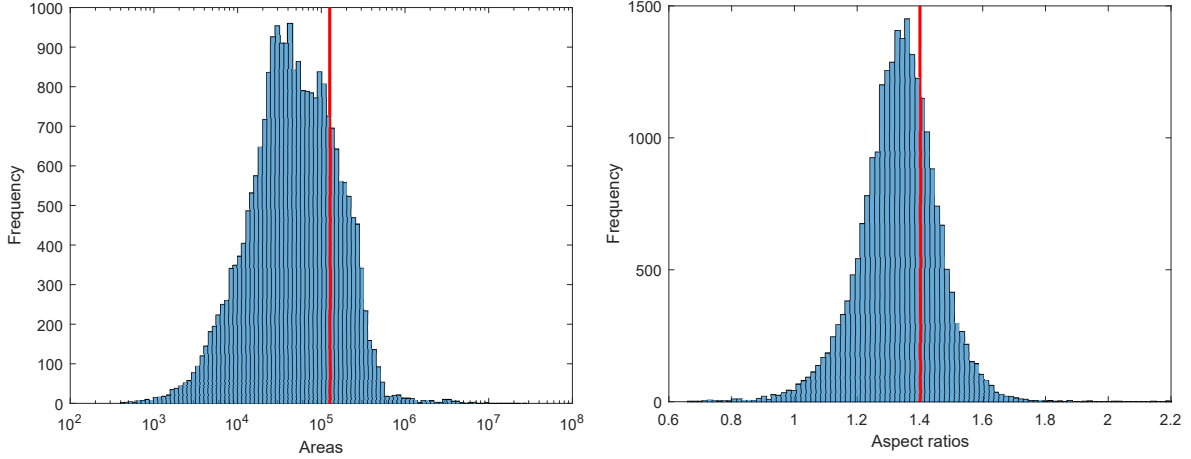


Figure 15: Areas (left) and aspect ratios (right) of the cropped faces using the ResNet-10 model applied to the UTKface wild faces dataset. The red lines mark the area and aspect ratio of the resized validation of 1.26×10^5 pixels² and 1.4, respectively.

Table 6: Error thresholds (in pixels) for the three significance levels.

	$\alpha = 0.50$	$\alpha = 0.05$	$\alpha = 0.01$
Static face mole	1.049	2.222	2.789
Static nose tip	1.425	2.968	3.683
Bike face mole	1.404	2.922	3.623
Bike nose tip	1.564	3.246	4.028
PD hand mole	1.219	2.571	3.225

sum of their squares is Chi square distributed

$$\delta x^2 + \delta y^2 \sim \chi^2.$$

The Cumulative Density Function (CDF) of each of the five conditions, is shown in Figure 21, generated by the *normal* function of the *random* number routines of *numpy* version 1.19.3 using Python 3.6. We use the CDF of the Chi-square distribution to determine the likelihood that an error stems from the manual labelling and establish error thresholds at the common 0.01, 0.05, and 0.5 significance levels (α). The human errors fall below these thresholds with probability 0.99, 0.95, and 0.5, respectively. The respective thresholds for all the three confidence levels can be seen in Table 6.

The test statistics described in Chi square analysis are described in Table 7 with the respective 99% confidence threshold to reject the null hypothesis of the errors coming from human labelling.

A.5 Calculation of SIFT descriptors

Figure 22 shows how SIFT descriptor are calculated from histograms of the magnitudes of the gradients of neighboring pixels. The magnitude of gradients around a 16×16 area around the keypoint are weighted using a Gaussian kernel. Histograms of the weighted magnitudes of each 4×4 area in the 16×16 area are created; resulting in 4×4 histograms. The bins in each 8-binned histogram represent the orientation of the gradients and the height of the bars represent the magnitude of that orientation. These histograms are concatenated into a vector of $4 \times 4 \times 8$ dimensions which represents the keypoint descriptor.

A.6 Approximations of Laplacian of Gaussians using box filters

SURF approximates the Laplacian of Gaussian using box filters. Figure 23 shows several examples of these approximations. Box filters is a cruder approximation of Gaussian second derivatives than the Difference of Gaussians used in SIFT (Lowe, 2004). However, the calculation of these box filter approximations is computationally cheap with the use of integral images, independently of their size.

A.7 Implementation of SIFT, SURF, and LK

We used SIFT, SURF, and LK as implemented in version 3.4.2.17 of OpenCV. For SIFT and SURF we used the `compute` function to calculate the feature descriptors of the given coordinate of the skin feature of interest in the reference frame.

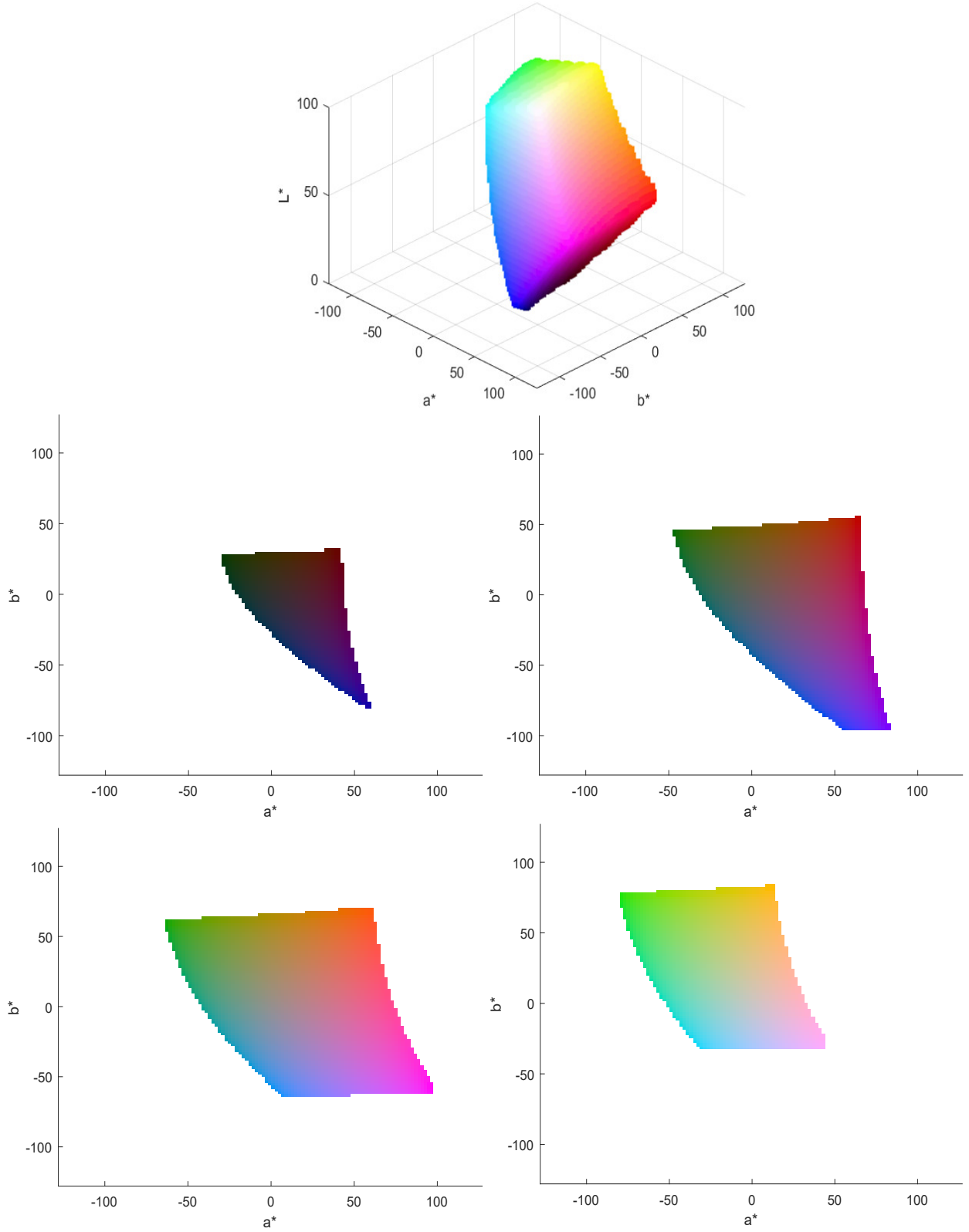


Figure 16: The CIELab color space. The color space has L^* value ranges of 0 to 100, a^* ranges from -127 to 127 , and b^* from -127 to 127 . The CIELab color space contains the entire RGB gamut (top). The a^* - b^* plane is shown at $L = 20$ (middle-left), $L = 40$ (middle-right), $L = 60$ (bottom-left) and $L = 80$ (bottom-right).

For LK we used the `calcOpticalFlowPyrLK` function to predict the location of the skin feature in the current frame. Details of our feature matching between the reference point and its closest match in the current frame are provided in Algorithm 1 for SIFT and SURF and Algorithm 2 for DFE. A detailed explanation of the methods implemented

in the functions `calculate_quadratic_surface_params()` and `get_subpixel_level_pred()` is given in section Subpixel level prediction in the manuscript. Location of the skin feature of interest in the current frame using LK is described in Algorithm 3. Note that we use Python notation for clarity of certain steps and assume the usage of OpenCV and Python functions.

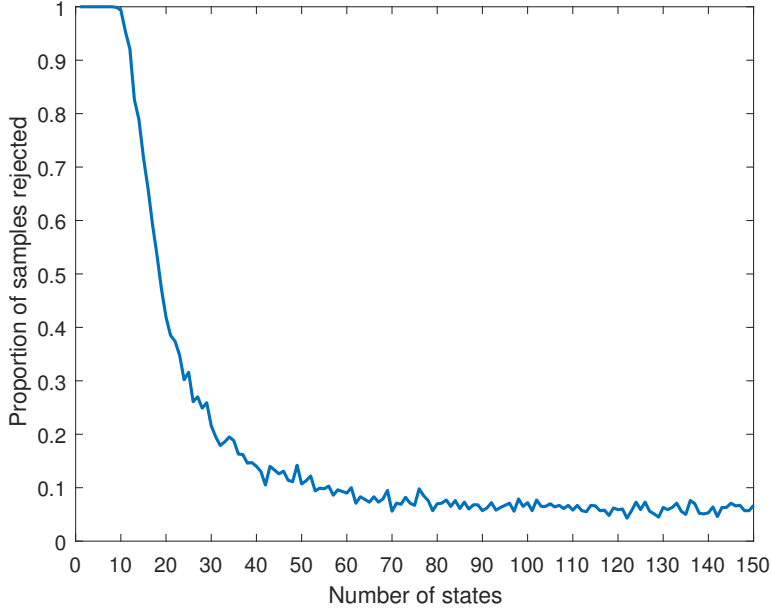


Figure 17: Proportion of samples for which the null hypothesis of the data coming from a normal distribution is rejected using the Lilliefors test at significance level 0.05 as a function of the number of states that the values were quantized into. All samples were drawn from a standard normal distribution.

Table 7: Test statistics for rejecting the null hypothesis of whether the errors are due to human errors. Statistics that fall below the threshold are in bold.

	SIFT	SURF	LK	DFE	Threshold
Static face mole	6.8887e+05	5.0428e+06	507.8146	467.2694	597.9500
Static nose tip	1.2527e+03	7.4170e+05	1.0507e+03	1.3334e+03	597.9500
Bike face mole	2.3114e+05	9.2964e+05	6.9858e+04	123.9379	401.4090
Bike nose tip	7.0651e+05	1.4756e+06	4.8984e+04	1.3331e+03	401.4090
PD hand mole	1.0317e+05	3.5759e+05	9.2540e+04	21.4238	109.9581

The default parameters specific to each method are described in their respective sections in the manuscript.

A.8 Weighted errors

We also weigh the errors e , *i.e.* distances between the prediction and the ground truth, of the validation set by their probability based on the CDF of the simulated Chi square distribution. The weighted error $e_{weighted}$ is defined as

$$e_{weighted} = \frac{e}{1 - F_{\chi^2}(e)},$$

where $F_{\chi^2}(e)$ is the CDF of the Chi square distribution evaluated at e . This weighting scheme penalizes errors that are inherent of the methods and not likely due to human mislabeling. The weighted errors for each condition can be seen in Table 8.

A.9 Maximum errors

The maximum errors for feature matching, *i.e.* tracking the original reference feature in the first frame, are found in Table 9. DFE achieves the lowest maximum error for all conditions except for tracking the face mole under static conditions. For this condition, the method with the lowest maximum error is LK followed by SIFT. Table 10 shows the maximum errors for tracking the prediction of the previous frame. For this tracking scheme, DFE was the method with the lowest maximum error for all conditions. This is because DFE was the only method that never diverged.

A.10 Tracking errors

A sudden increase in the tracking error shown in Figure 7 occurs for frames 43 to 46 for DFE for tracking the nose tip under bike conditions. This is the only condition for which we can see this sudden increase in the tracking error for DFE. A sudden increase in the error of LK, another method that performed well in most circumstances, also appears in the same frames. A slightly smaller increase is seen in Figure 8 for the same frames for DFE. This suggests these frames are of interest as they are the first frames for which we can see a clear drop in performance. Thus we decided to investigate this drop.

We plotted frames 43 to 46 (in chronological order) along side the original frame in Figure 24. We also plotted the enlarged 160×160 window around the reference crop and the difference between the reference crop and other windows of the same dimensions in the frames 43 to 46 in grayscale. These are similar to the observation window of LK with the parameters used in our experiments, *i.e.* window size of 10×10 and a L_m of 4.

Figure 25 shows the distance between the ground truth and the original reference image and the distances of LK and DFE methods for tracking the nose tip under bike condition temporally. We believe that the large error from LK is due to the ground truth having a very large displacement from the original feature. This displacement causes the new feature to be deformed and thus making the optical flow equations hard to solve. As mentioned previously, an assumption from the LK method is that the motion is small (Lucas and Kanade, 1981). The error in LK has a correlation coefficient of 0.52 with the distance of the ground truth to the original reference feature. Determining whether a correlation is strong is subjective but

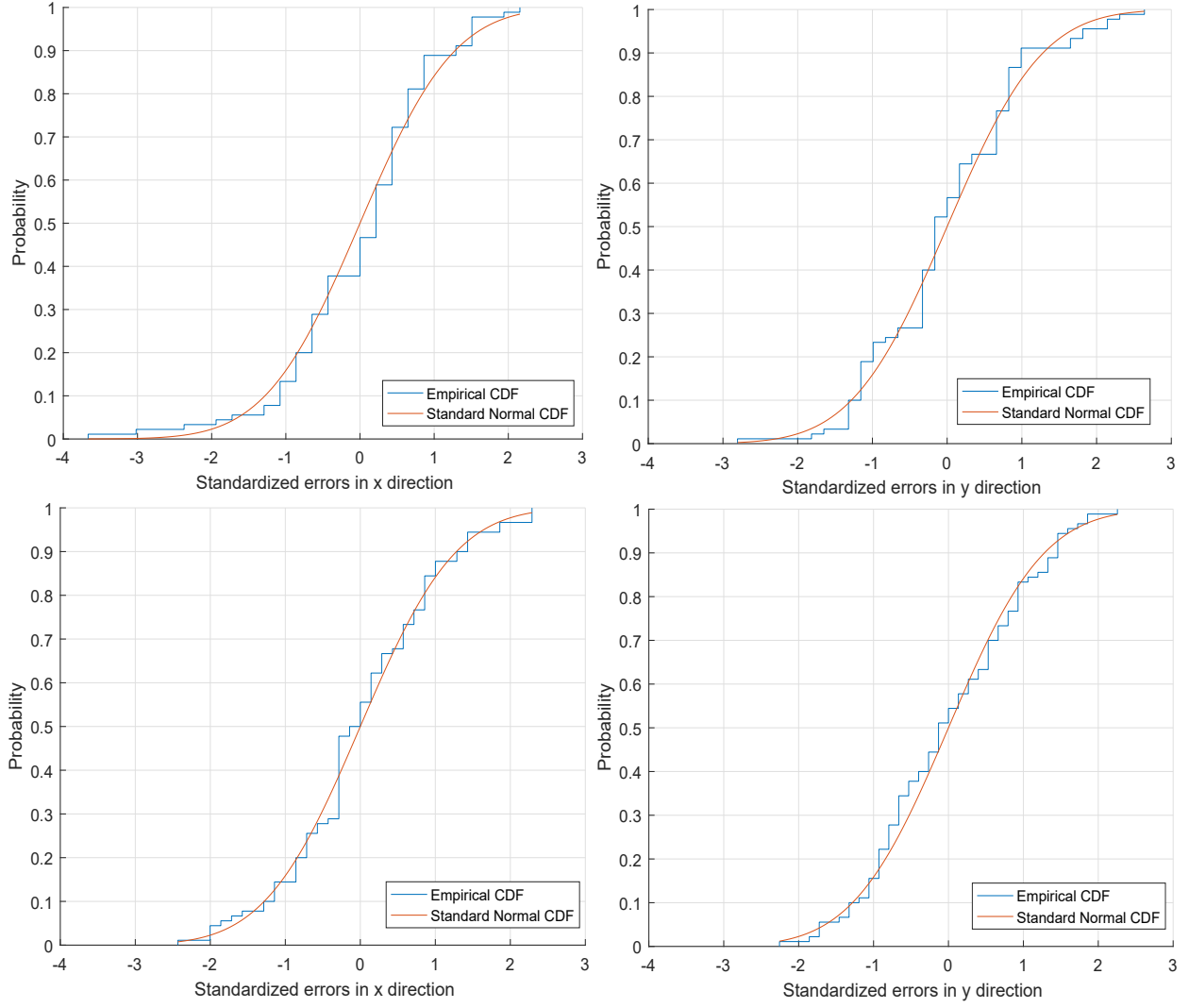


Figure 18: CDF of the standardized errors from the videos of static conditions in x direction for face mole (top-left), errors in y direction for face mole (top-right), errors in x directions for nose tip (bottom-left), and errors in y direction for nose tip (bottom-right). The quantized errors were standardized by dividing them by their respective standard deviation. The red line marks the theoretical CDF of a standard normal distribution.

Table 8: Weighted mean errors – the original error weighted by the reciprocal of the significance level of the simulated Chi square distribution. The best results are highlighted in bold.

	SIFT	SIFT with threshold	SURF	LK	DFE
Static face mole	1.63×10^7	1.87×10^8	1.72×10^8	1.02×10^2	6.14×10^1
Static nose tip	6.05×10^4	3.14×10^8	1.63×10^8	3.75×10^4	6.35×10^4
Bike face mole	1.56×10^7	1.76×10^8	1.36×10^8	3.83×10^6	2.34×10^1
Bike nose tip	6.29×10^7	3.45×10^8	2.57×10^8	9.40×10^6	1.11×10^5

Table 9: Maximum errors for feature matching. The best results are highlighted in bold.

	SIFT	SIFT with threshold	SURF	LK	DFE
Static face mole	210.2243	516.1395	265.0907	2.2168	2.1347
Static nose tip	5.6971	516.1395	139.7204	5.1310	5.7030
Bike face mole	218.5698	516.1395	207.2922	254.7781	2.0818
Bike nose tip	79.6503	516.1395	206.8976	76.3600	6.4795
PD hand mole	219.8465	516.1395	200.1399	120.3210	1.5241

a correlation coefficient above 0.5 is often considered moderate to strong (Akoglu, 2018). Thus we believe this to in part explain the large errors.

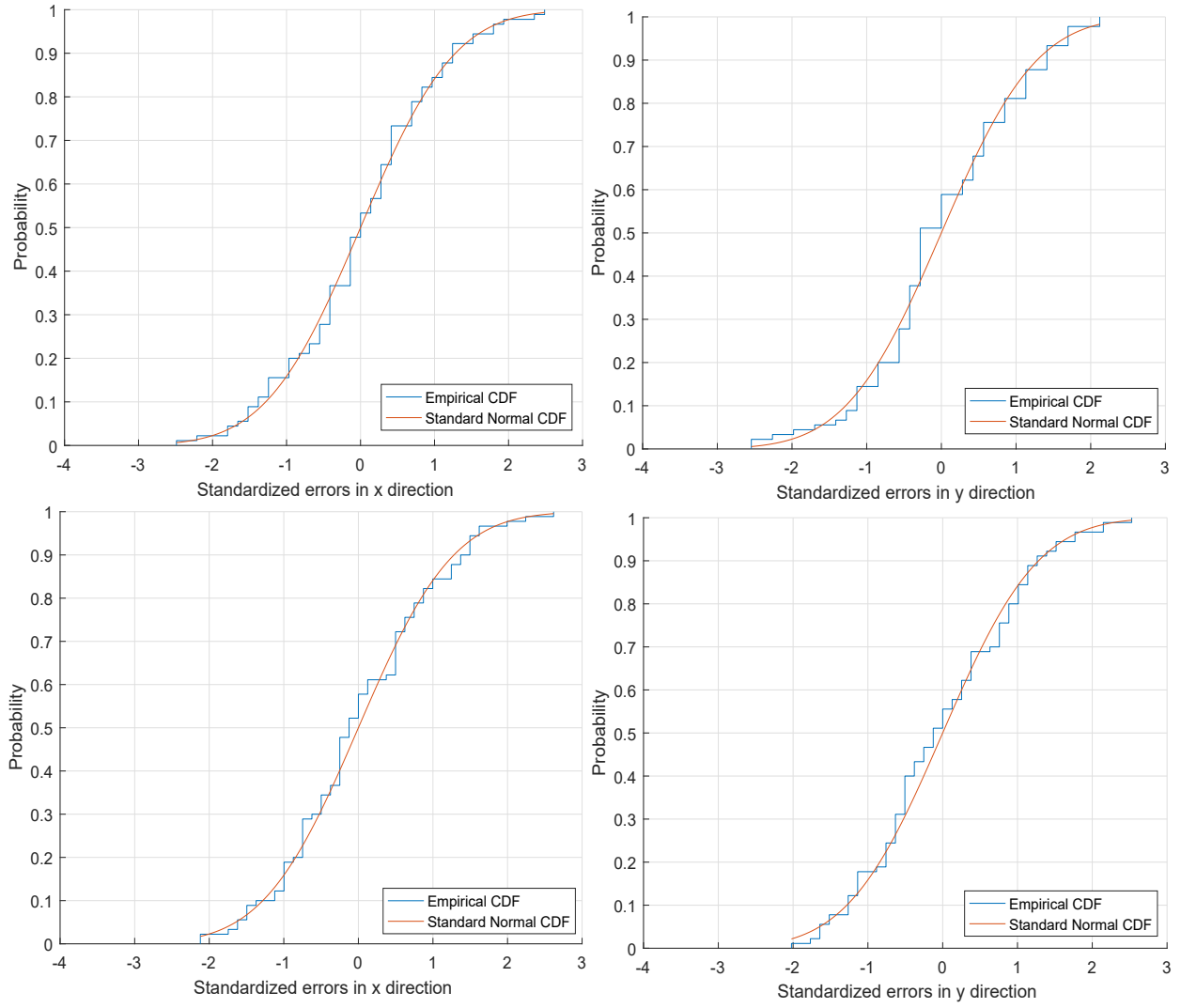


Figure 19: CDF of the standardized errors from the videos of bike conditions in x direction for face mole (top-left), errors in y direction for face mole (top-right), errors in x directions for nose tip (bottom-left), and errors in y direction for nose tip (bottom-right). The quantized errors were standardized by dividing them by their respective standard deviation. The red line marks the theoretical CDF of a standard normal distribution.

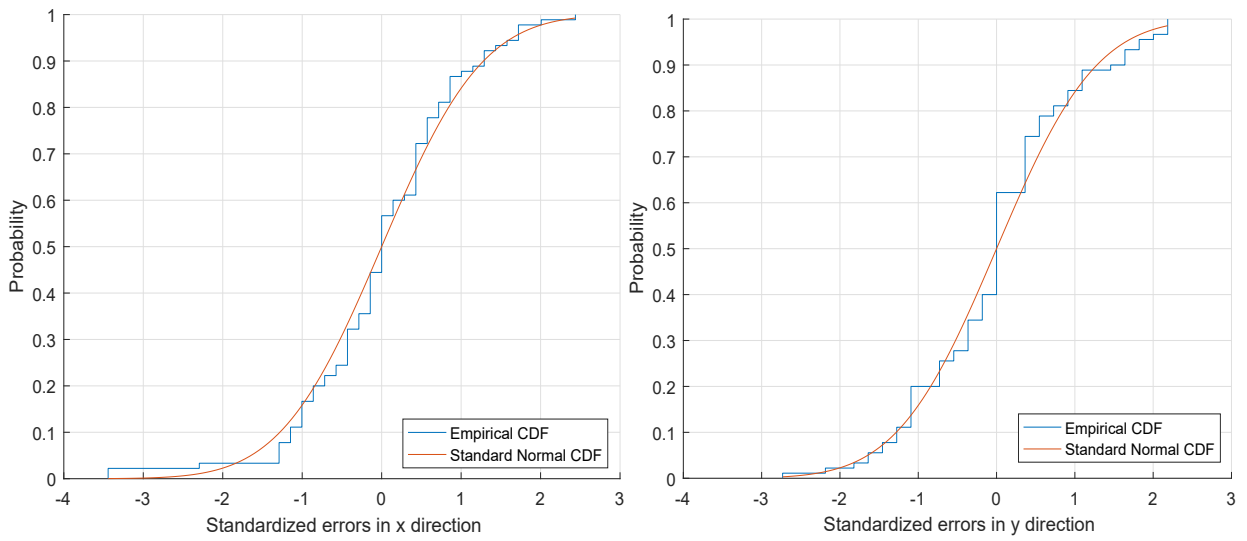


Figure 20: CDF of the standardized errors from the videos of PD condition in x direction for hand mole (left) and errors in y direction for hand mole (right). The quantized errors were standardized by dividing them by their respective standard deviation. The red line marks the theoretical CDF of a standard normal distribution.

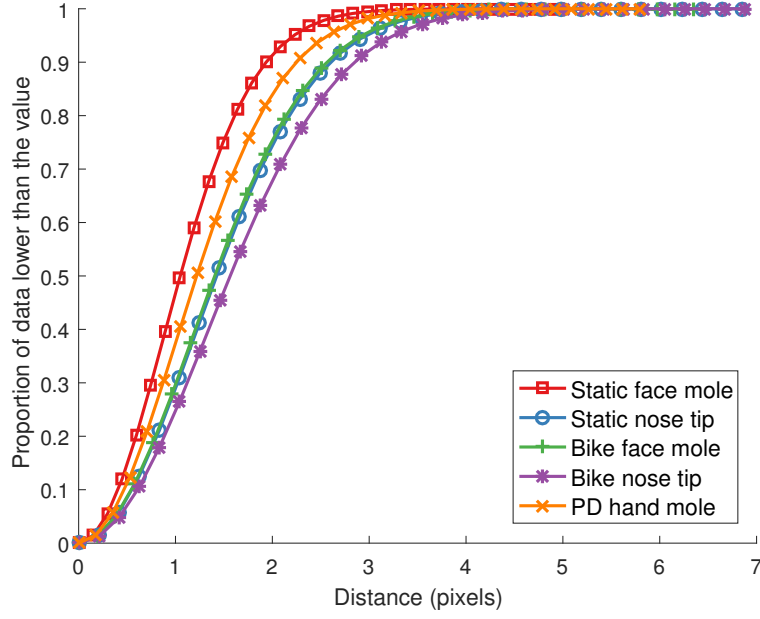


Figure 21: Simulated cumulative distribution functions for each of the body part and motion conditions.

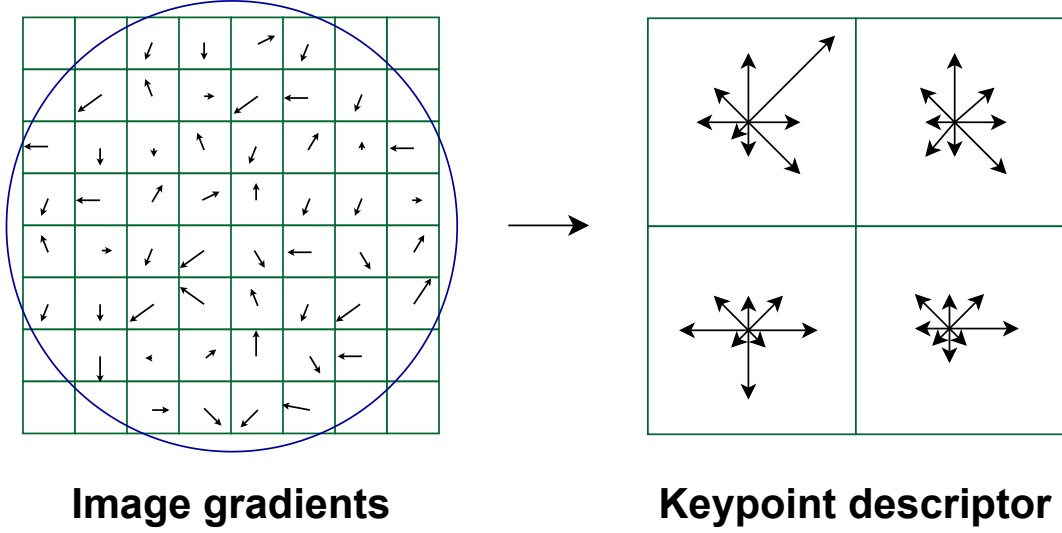


Figure 22: Calculation of the SIFT descriptor through the histogram of the magnitudes and gradients of neighboring pixels. The neighboring pixels are smoothed using a Gaussian filter (blue circle). The magnitudes and gradients are then accumulated and represented as histograms for each of the sub-regions. The length of each arrow in the sub-sampled space corresponds to the sum of the gradient magnitudes near that direction within that region. This figure shows a 2×2 descriptor array computed from an 8×8 set of samples, whereas the original publication (Lowe, 2004) use a 4×4 descriptor array computed from a 16×16 sample array.

Table 10: Maximum errors for tracking the prediction from the previous frame. The best results are highlighted in bold.

	SIFT	SIFT with threshold	SURF	LK	DFE
Static face mole	266.1209	516.1395	277.9227	263.1993	5.4279
Static nose tip	250.1239	516.1395	265.6182	287.4956	9.5427
Bike face mole	282.1509	516.1395	319.0986	346.0556	4.8943
Bike nose tip	304.4242	516.1395	325.6847	293.7723	5.1006
PD hand mole	231.5862	516.1395	276.3275	354.3394	3.2052

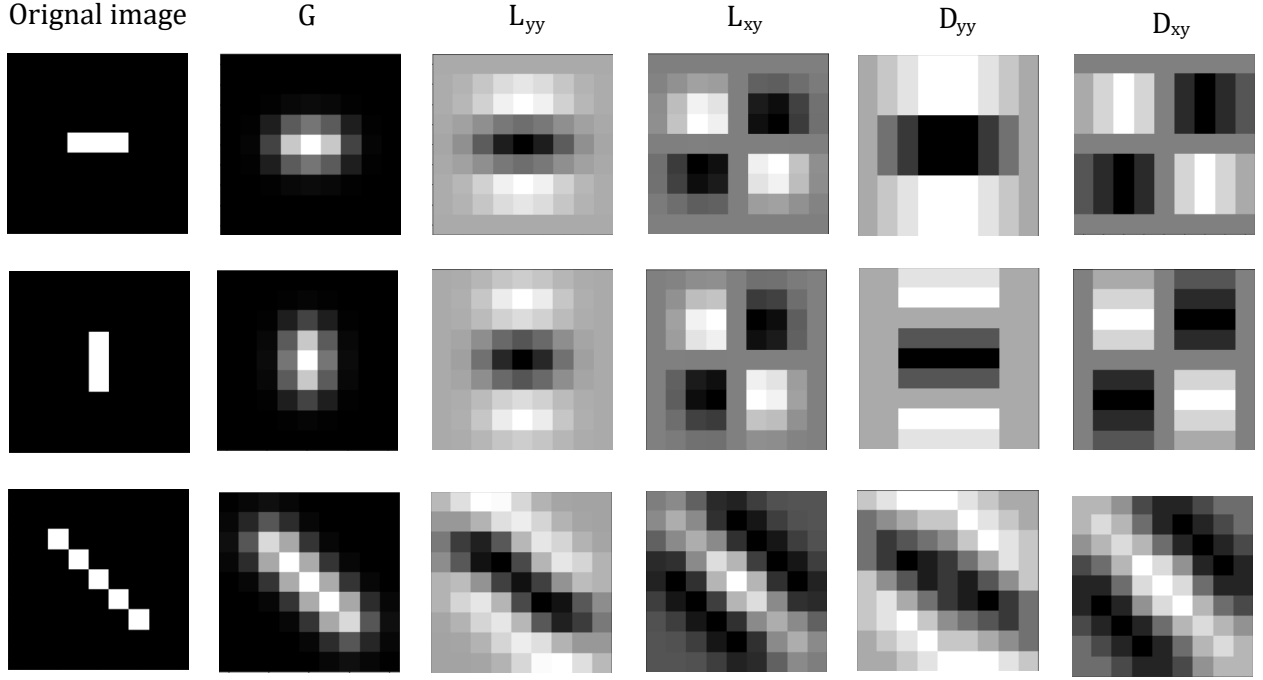


Figure 23: Examples of approximation of second derivatives using box filters. L_{yy} is the second derivatives in y direction of the Gaussian convolved image G , L_{xy} is the second derivative first in x direction and then in y direction of the Gaussian convolved image G , D_{yy} is the approximation of L_{yy} using a box vertical filter, and D_{xy} is the approximation of L_{xy} using a box diagonal filter in.

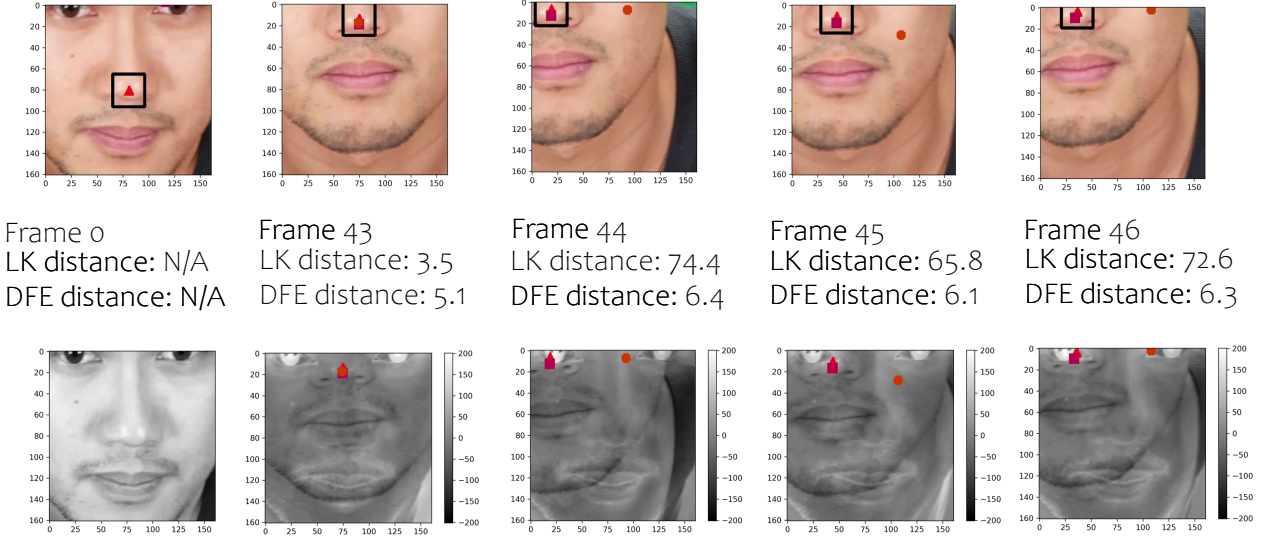


Figure 24: Original frame and the first frames with large error for tracking the nose tip under bike conditions. Each frame is accompanied by a 160×160 difference map of corresponding image and the reference crop. The ground truth is marked by a red triangle, the LK prediction is marked by an orange circle and the DFE prediction is marked by a purple square.

A.11 Nearest neighbors to second nearest neighbor distance ratios

In SIFT a set of keypoints from one image is matched to a set of keypoints in another image by comparing the L2 norm of their residuals (Lowe, 2004). Merely using the global minimum of the L2 norm produces a lot of false positive matches for the high-dimensional descriptors used in SIFT. Lowe resorted to matching keypoints only if the ratio of the descriptor distances, *i.e.* square root of the SSR, between the nearest neighbor and second nearest neighbor is lower than 0.8. The threshold of 0.8 is an experimental result after comparing the PDF of correct matches versus the PDF of incorrect matches for different closest to second closest nearest neighbor distances on a database of 40,000 keypoints. For their object recognition implemen-

tation, the threshold eliminated 90% of false matches while discarding less than 5% of the correct matches. This strategy works well because matches need to have the closest neighbor significantly closer than the closest incorrect match to achieve a reliable matching, hence making the algorithm more robust. For this reason we decided to also investigate the nearest and second nearest neighbor distances.

Figure 26 show the spatial distance to the ground truth of the nearest and second nearest neighbors as a function of their descriptor distances in the 128-dimensional latent feature space with respect to the reference descriptor for our DFE method, *i.e.* the square root of the SSR. In 56% of the images, the spatial distance between the ground truth and the second nearest neighbor is larger than that of the nearest neighbor. In 90% of the images, the largest spatial distance between any of the

Algorithm 1 Feature matching using SIFT and SURF to locate the skin feature.

Require: $\text{ref}_{\text{point}}$, $\text{img}_{\text{reference}}$, $\text{img}_{\text{current}}$

Ensure: pred ▷ Location of best match

1: $\text{size}_{\text{window}} = (31, 31)$, $\text{stride} = 1$ ▷ Initialize parameters

2: $\text{positions} = []$, $\text{curvatures} = []$, $\text{candidates} = []$

3: $\text{descriptor} = \text{cv2.xfeatures2d.method_create}()$ ▷ Create SIFT/SURF object by replacing “method” in the function name by SIFT/SURF

4: $\text{ref}_{\text{descriptor}} = \text{descriptor.compute}(\text{img}_{\text{reference}}, \text{ref}_{\text{point}})$ ▷ Get reference descriptor

5: **for** ($i < \text{int}((\text{img}_{\text{current}}.\text{shape}[0] - \text{size}_{\text{window}}[0]) / \text{stride})$) **do** ▷ Generate list of possible positions

6: **for** ($j < \text{int}((\text{img}_{\text{current}}.\text{shape}[1] - \text{size}_{\text{window}}[1]) / \text{stride})$) **do**

7: $x = \text{int}(j + \text{ceil}(\text{size}_{\text{window}}[1] / 2))$

8: $y = \text{int}(i + \text{ceil}(\text{size}_{\text{window}}[0] / 2))$

9: $\text{positions.append}([y, x])$ ▷ Get all possible positions where a 31×31 window can be centered

10: **end for**

11: **end for**

12: $\text{descriptors} = \text{descriptor.compute}(\text{img}_{\text{current}}, \text{positions})$

13: $\text{ssrs} = \text{sum}((\text{descriptors} - \text{ref}_{\text{descriptor}})^2, \text{axis}=1)$ ▷ Row-wise calculation of SSRs

14: **for** $\text{error}_{\text{unique}}$ in $\text{unique}(\text{sort}(\text{ssrs}))$ **do** ▷ Filter out points by their curvature

15: **for** candidate in $\text{where}(\text{ssrs} == \text{error}_{\text{unique}})$ **do**

16: $c = \text{calculate_quadratic_surface_params}(\text{positions}[\text{candidate}], \text{img}_{\text{current}})$ ▷

 Get the 6 parameters of the surface fitted to the 3×3 neighborhood around the candidate point. See section Subpixel level prediction.

17: $D = 4c[5]c[4] - c[3]^2$

18: **if** $D > 0$ and $c[4] > 0$ **then** ▷ Check if the fitted surface has a local minimum

19: $\text{curvatures.append}(D)$

20: $\text{candidates.append}(\text{candidate})$

21: **end if**

22: **end for**

23: **if** $\text{bool}(\text{curvatures})$ **then**

24: **break** ▷ Stop if a point fulfills the local minimum criteria

25: **end if**

26: **end for**

27: $\text{pred}_{\text{pixel}} = \text{positions}[\text{candidates}[\text{argmax}(\text{curvatures})]]$ ▷ Predicted position with pixel accuracy

28: $\text{pred} = \text{get_subpixel_level_pred}(\text{pred}_{\text{pixel}}, \text{img}_{\text{current}})$ ▷ Predicted position with subpixel accuracy. See section Subpixel level prediction.

first two neighbors and the ground truth is smaller than 4.4 pixels. The largest spatial distance among the first two neighbors, shown for tracking the nose tip in bike conditions, is just 8 pixels. The largest distance of the first two neighbors is larger for the nose tip than for the face mole, reflecting the fact that it is a less distinct feature. For the static conditions, our method can achieve a lower nearest neighbor to second nearest neighbor ratio than for the bike conditions. For the bike conditions, a large portion of the ratios is close to one. This is not surprising, as for the bike conditions the deformation is larger and thus the point is harder to recognize across frames.

The distributions of the ratios of the nearest to second nearest neighbor distances for DFE are in Figure 27. The smallest average mean ratio is for tracking the nose tip under static conditions and the largest mean ratio is for the nose tip under bike conditions.

Interpretation of the ratio of the nearest to second nearest neighbor distances is complicated by the fact that a large ratio can occur for different reasons. In the case of a highly distinctive feature, characterised by a small spatial change leading to a large change in the feature descriptor, a large ratio would occur if the center of the feature occur midway between two pixels. The SSR at both these pixels would then be significantly larger than the SSR of the center, but similar and seen as a ratio near one. In the case of a second skin feature that locally is very similar to the one of interest but at a different location, the ratio would also be large. Since we only evaluate the SSR with pixel level accuracy when calculating these

ratios, we cannot distinguish this case from a case of having two similar skin features at different location in the image with similar SSR. In the former case a high ratio is good, while in the latter case it is problematic since noise could cause the SSR of the wrong skin feature to be lower than the one of interest and thus a large tracking error. In the case of a not so distinctive feature, characterised by a small spatial change leading to a small change in the feature descriptor, the ratio of all points surrounding the center point of the feature will be large. When tracking this feature, the large ratio increases the robustness because a small spatial error results from matching with one of the neighbouring pixels in some images. At the same time, the feature cannot be precisely located due to the low curvature of the local SSR landscape. Taken together these cases highlight the fact that sometimes a high ratio and sometimes a low ratio is desired. For DFE, we have observed local convexity of the SSR landscape around the skin features we have validated it on. Thus a moderate nearest neighbor to second nearest neighbor ratio is desired because moving just one pixel from the best match should give a fair match and a similar SSR at the same time a distinction to the best match is desired. This makes the prediction of the location of the reference feature, which at pixel-level is a result of a feature matching task work better using our subpixel level method.

Algorithm 2 Feature matching using DFE to locate the skin feature.

Require: ref_point , img_reference , img_current , encoder **Ensure:** pred

▷ Location of best match

▷ Initialize parameters

▷ Create reference

▷ Get reference descriptor

▷ Generate list of possible positions

▷ Row-wise calculation of SSRs

▷ Filter out points by their curvature

▷ Get the 6 parameters of the fitted surface around the 3×3 neighborhood around the candidate point. See section Subixel level prediction.

▷ Check if the fitted surface has a local minimum

▷ Stop if a point fulfills the local minimum criteria

▷ Predicted position with pixel accuracy

▷ Predicted position with subpixel accuracy. See section Subixel level prediction.

Algorithm 3 Location of the skin feature in the current frame using LK.

Require: ref_point , img_reference , img_current **Ensure:** pred

▷ Location of best match

▷ Required parameters for LK.

A.12 Nearest neighbors within an acceptable distance threshold

We also investigated the sensitivity of the methods to the selection of nearest neighbors within the distance threshold defined by the 99% CI of the simulated Chi-square distribution. We refer here to the spatial distance (in pixels) between the ground truth and the nearest neighbor. For each frame, we investigated the nearest neighbor rank, sorting by the distance of the neighbors to the ground truth point in ascending order, of the first point to fall outside of the threshold for SIFT, SURF, and DFE. Figure 28 shows the number of nearest neighbors that fall within this spatial distance threshold for all conditions. Our method is superior to SIFT and SURF in all conditions, having more nearest neighbors close to the ground truth. This

implies that even when our method localizes a point incorrectly, it still typically selects a point in the neighborhood of the ground truth. This implies that DFE is more precise since the neighbors are closer to each other. From Figure 6, we know that DFE typically is more accurate, since the error to ground truth is the smallest.

A.13 Spatial SSR landscape

Similarly to Figures 12, 30, and 31; we in Figure 29 observe that the SSR landscape of our method contains an organized structure, contrary to SIFT and SURF, which appear to have a random structure. We plotted the SSR as a function of spatial conditions of the image for the 15th largest error for track-

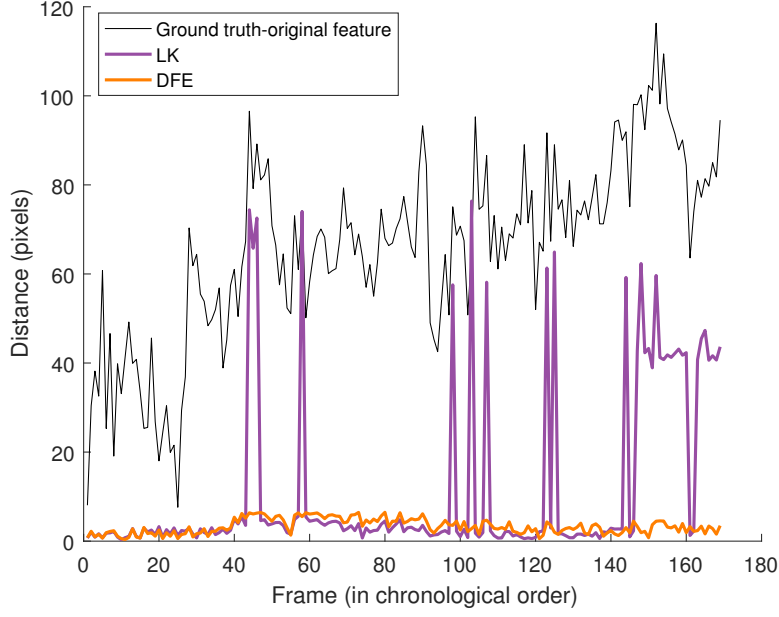


Figure 25: Distance between the ground truth and the original reference image and the distances of LK and DFE methods for tracking the nose tip under bike conditions. The correlation coefficient for the errors of LK and DFE are 0.52 and 0.33, respectively.

ing the face mole under bike conditions. We chose this image because it is a case in which DFE performs well, achieving the lowest error of 1.73 pixels, while SIFT and SURF perform poorly. It is hence an example where accurate feature matching is possible.

In addition, we also calculated the SSR landscape of the largest errors and smallest sum of localization errors in Figures 30 and 31, respectively. For the worst cases the localization error is the worst globally among all body part-motion combinations. The cumulative error for the image with smallest sum of localization errors is 2.786 pixels for tracking the face mole under bike conditions. Similarly to Figure 12 and Figure 30, only the DFE show an organized structure. SIFT and SURF have landscapes that seem random and irregular. The generalisations to the PD data are seen in Figures 32 and 33 for the largest errors and smallest sum of localization errors, respectively.

A.14 Algorithm errors

The proportion of images for which the hypothesis that the error is due to human labelling of the ground truth can be rejected as a function of significance level reveals when the error is likely due to the algorithm. Figure 34 shows the proportion of images in each of the four validation cases below each possible significance threshold established by our Chi square analysis. The error in a large proportion of the images is unlikely to be due to human labelling of the ground truth, especially for SIFT and SURF, while it is likely to be due to human labelling for DFE. A low line at all points in these figures is a hallmark of the good performance of a method.

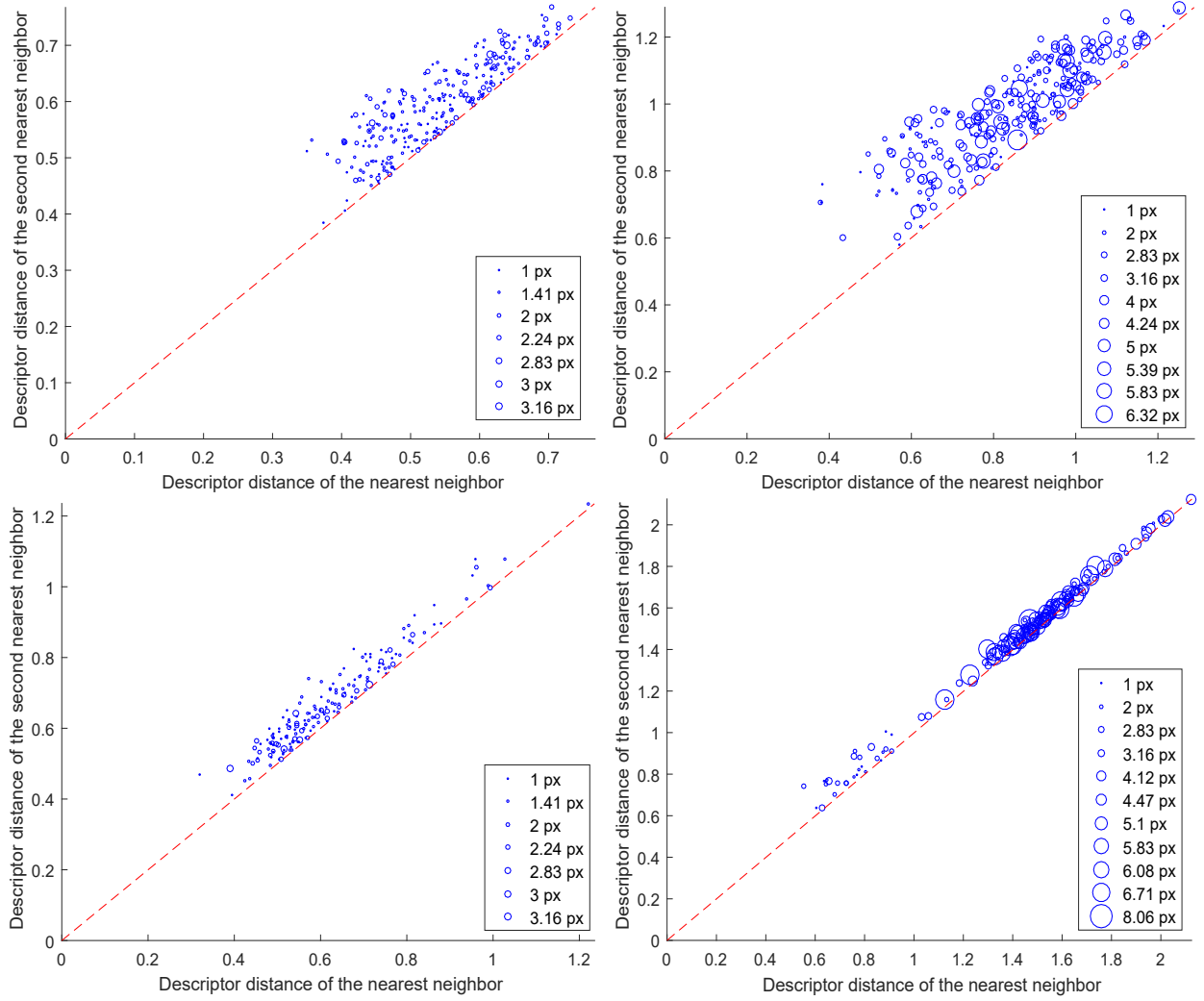


Figure 26: Distance of the second nearest neighbor as a function of the distance of the nearest neighbor for matching the face mole under static conditions (top-left), nose tip under static conditions (top-right), face mole under bike conditions (bottom-left) & nose tip under bike conditions (bottom-right). The descriptor distance of the nearest neighbors refers to the distance of the high dimensional representations between the reference point and the closest matching features in the image. The size of the markers is proportional to the largest spatial distance of the two neighbors to the ground truth. The red dashed line marks the $x = y$ line.

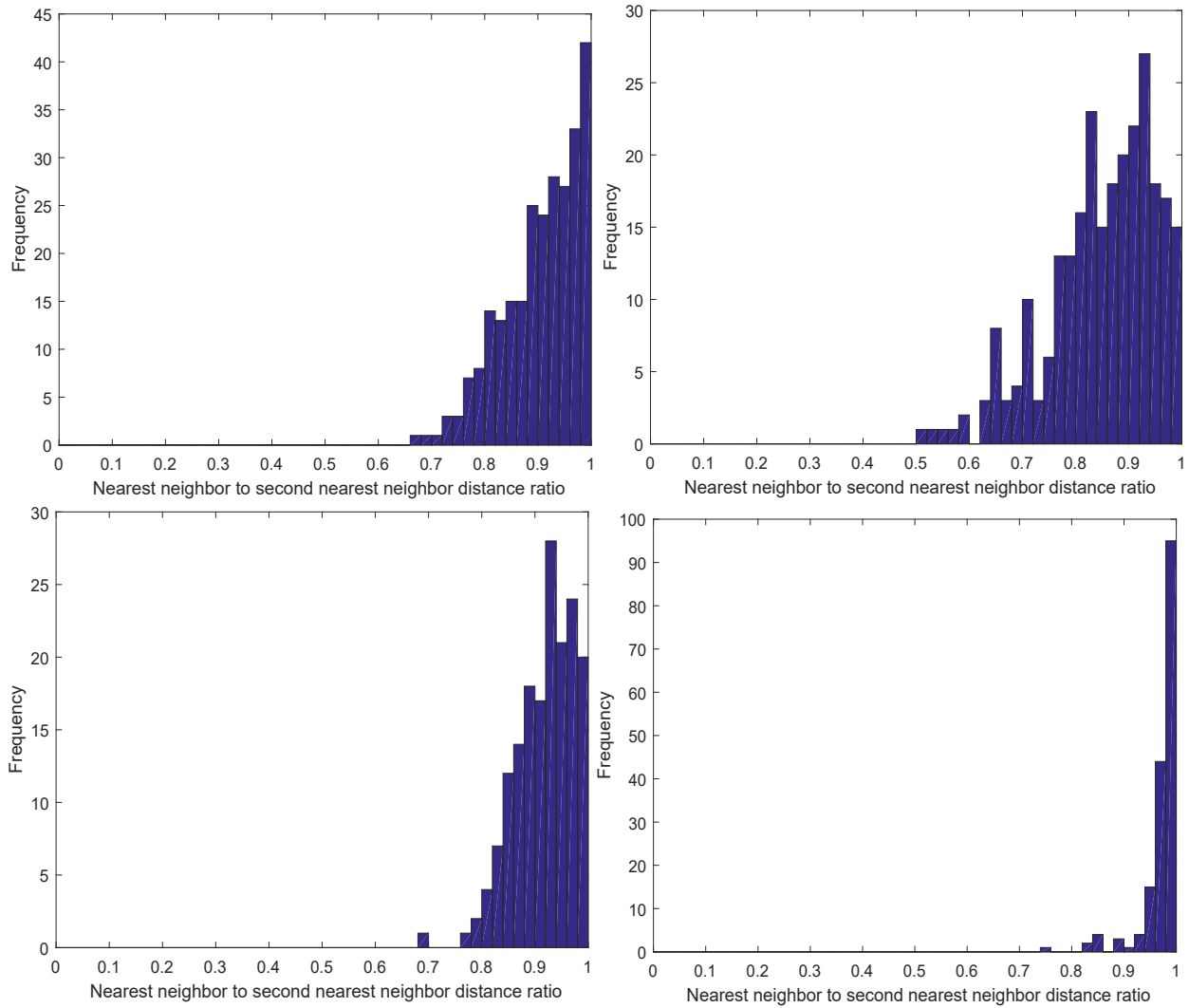


Figure 27: Distribution of the ratios of the nearest to the second nearest neighbor distances for matching the face mole under static conditions (top-left), nose tip under static conditions (top-right), face mole under bike conditions (bottom-left) & nose tip under bike conditions (bottom-right). The mean ratios are 0.9065, 0.8504, 0.9174, and 0.9718; respectively.

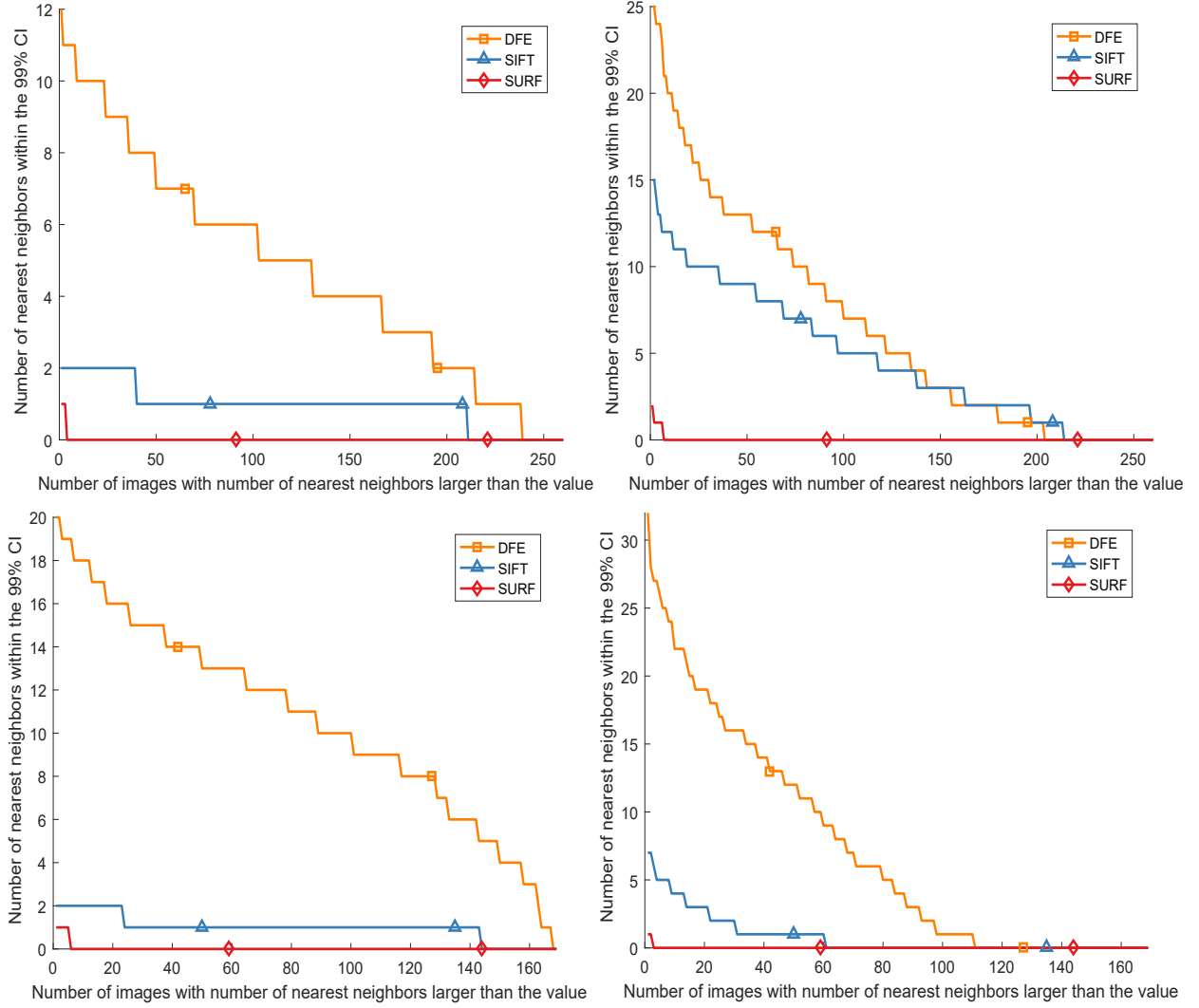


Figure 28: Number of nearest neighbors within the 99% CI for tracking the face mole under static conditions (top-left), nose tip under static conditions (top-right), face mole under bike conditions (bottom-left), and nose tip under bike conditions (bottom-right). The distances of the nearest neighbors are calculated at a pixel level resolution.

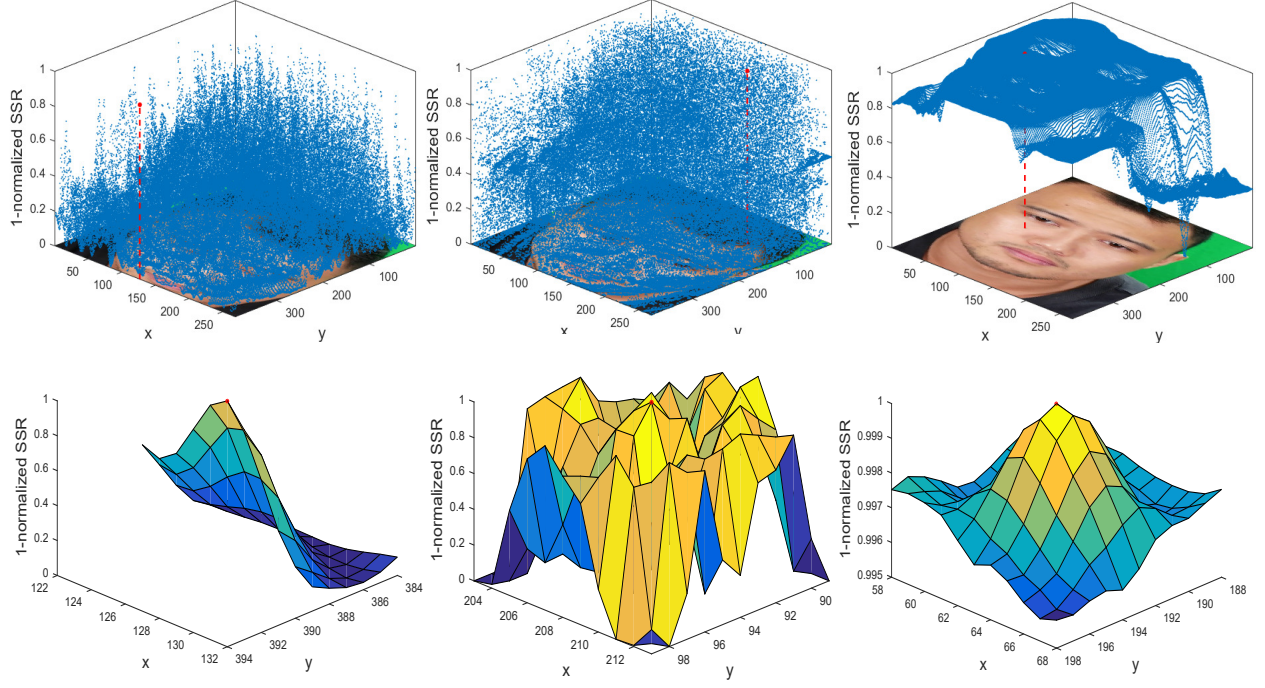


Figure 29: SSR of the frames with the 15th largest SSR value for tracking the face mole under bike conditions as a function of the spatial image coordinates for SIFT (left), SURF (middle), and DFE (right) and their corresponding regional enlargements of the optimum. The red dashed lines mark the point with minimum SSR. The distances to the ground truth are 95.65, 212.41, and 1.73 pixels, respectively. Both SIFT and SURF perform poorly while DFE performs well.

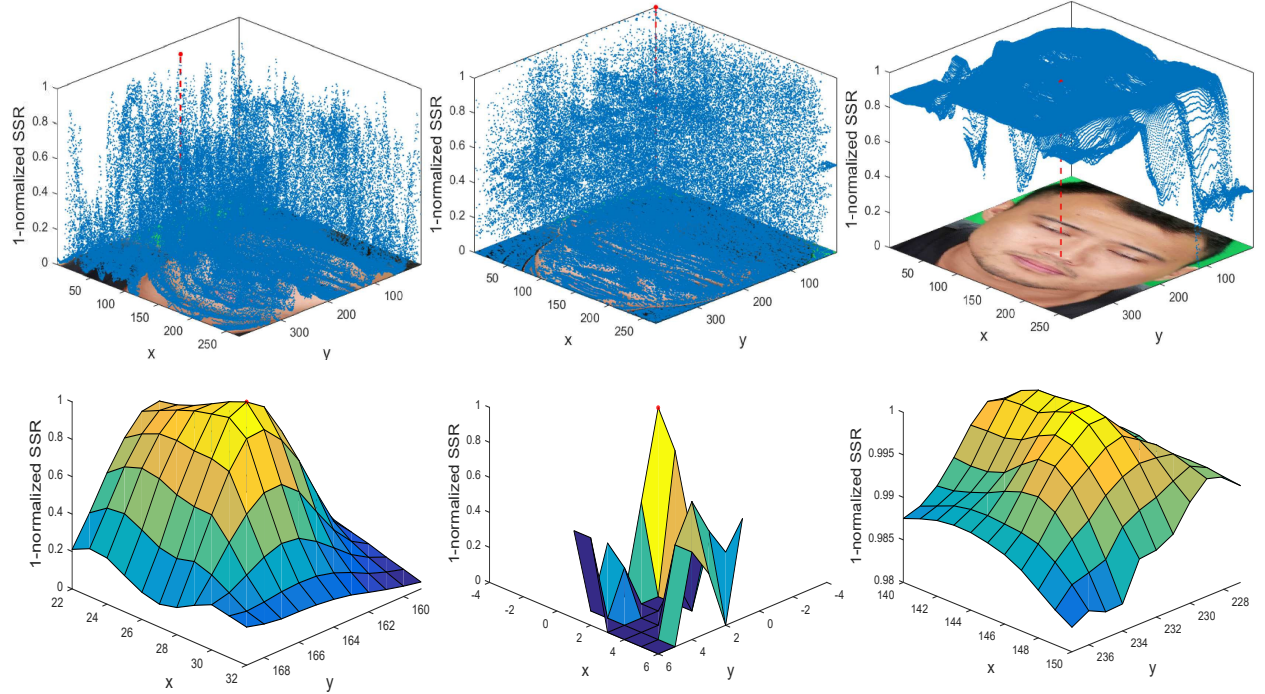


Figure 30: SSR as a function of the spatial image coordinates for the images with the largest localization errors for nose tips under bike conditions for SIFT (left), SURF (middle), and DFE (right) and the regional enlargements of the optimum. The red dashed lines mark the point in the space with minimum SSR, which is plotted as a red circle. The distances to the ground truth are 179.65, 355.45, and 6.48 pixels, respectively.

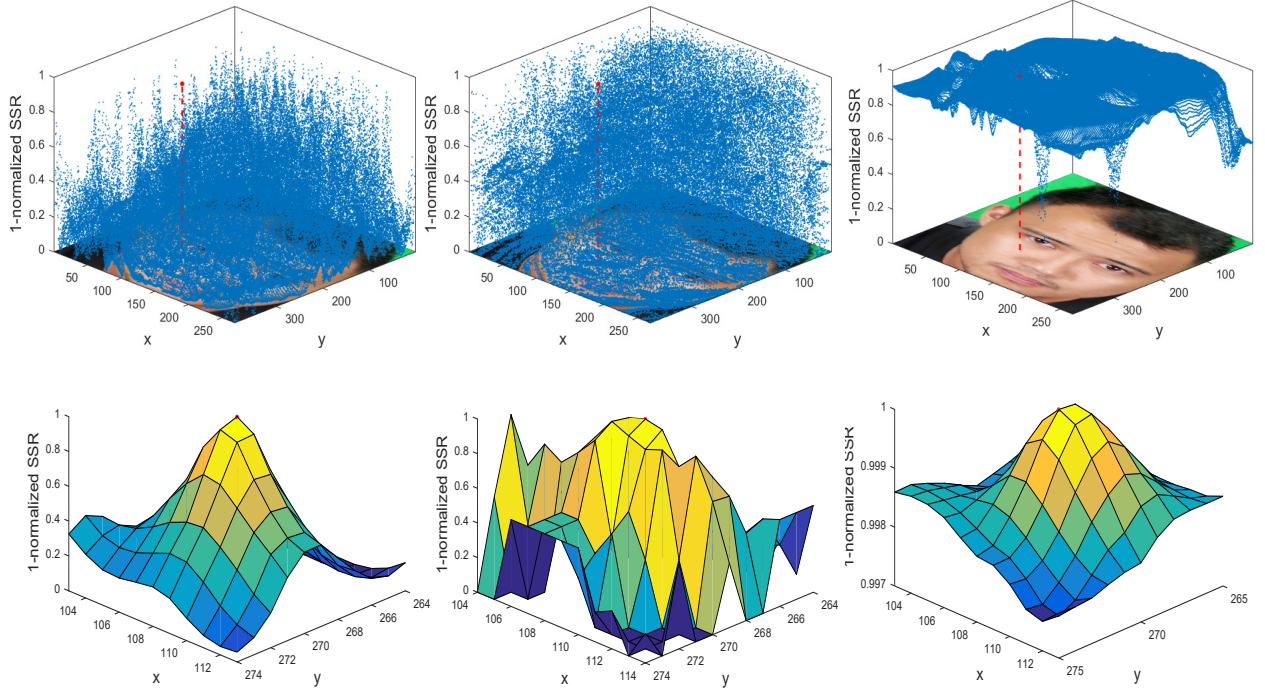


Figure 31: SSR as a function of the spatial image coordinates for the single image with the smallest sum of localization errors across SIFT (left), SURF (middle), and DFE (right) for tracking the face mole under bike conditions and their corresponding regional enlargements. The red dashed lines mark the point with minimum SSR. The distances to the ground truth are 0.89, 1.00, and 0.89 pixels, respectively.

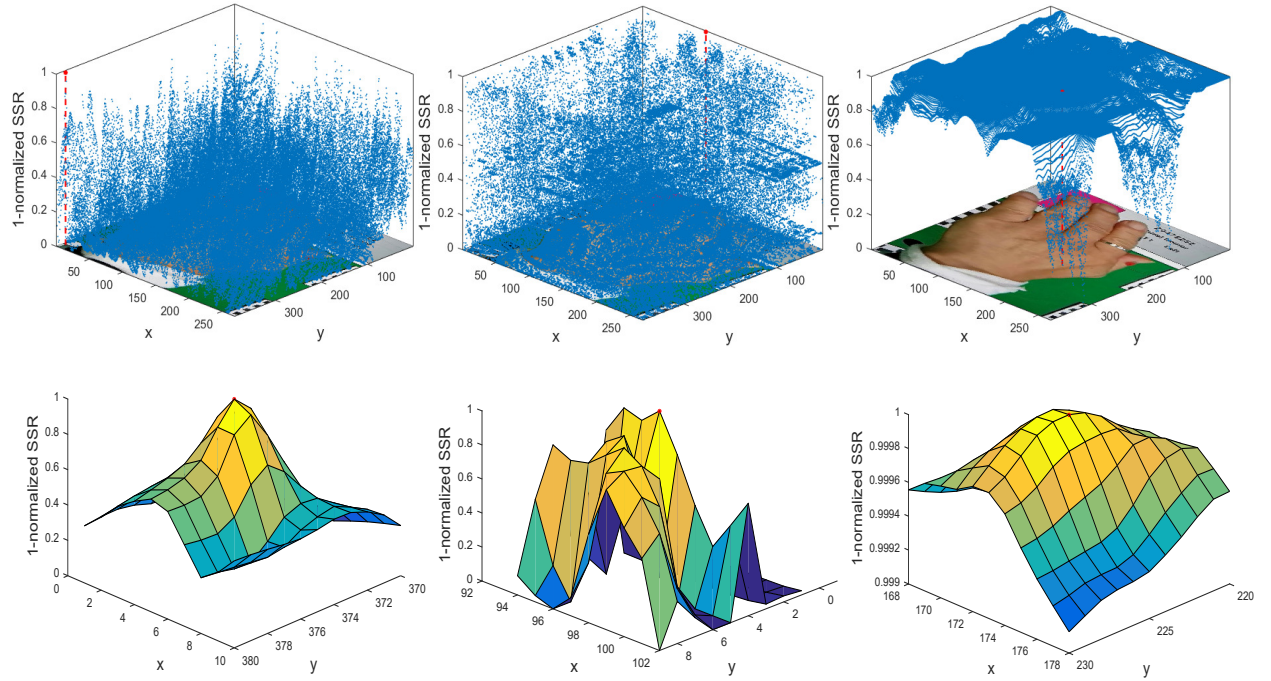


Figure 32: SSR as a function of the spatial image coordinates for the images with the largest localization errors for tracking the moles in the hand of the PD patient for SIFT (left), SURF (middle), and DFE (right) and their corresponding regional enlargement of the optimum. The red dashed lines mark the point with minimum SSR. The distances to the ground truth are 219.85, 242.34, and 1.52 pixels, respectively.

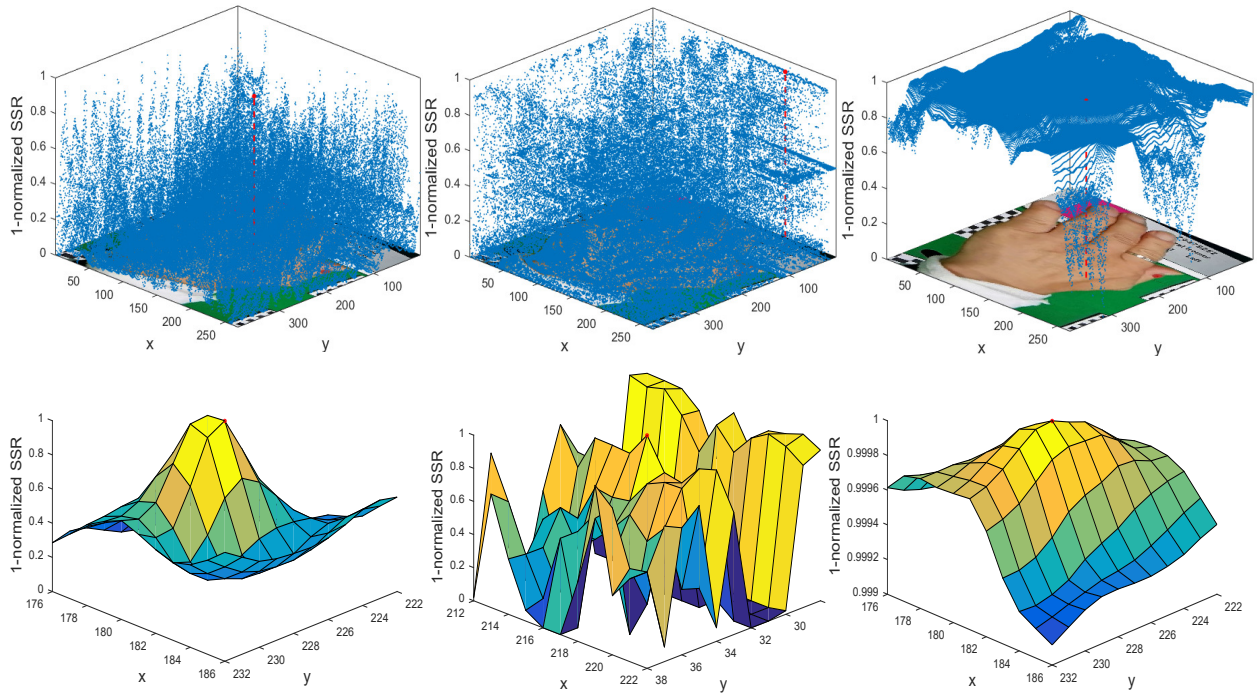


Figure 33: SSR as a function of the spatial image coordinates for the single image with the smallest sum of localization errors for tracking the mole on the hand of the PD patient for SIFT (left), SURF (middle), and DFE (right) and their corresponding regional enlargements of the optimum. The red dashed lines mark the point with minimum SSR. The distances to the ground truth are 1.55, 196.12, and 1.41 pixels, respectively.

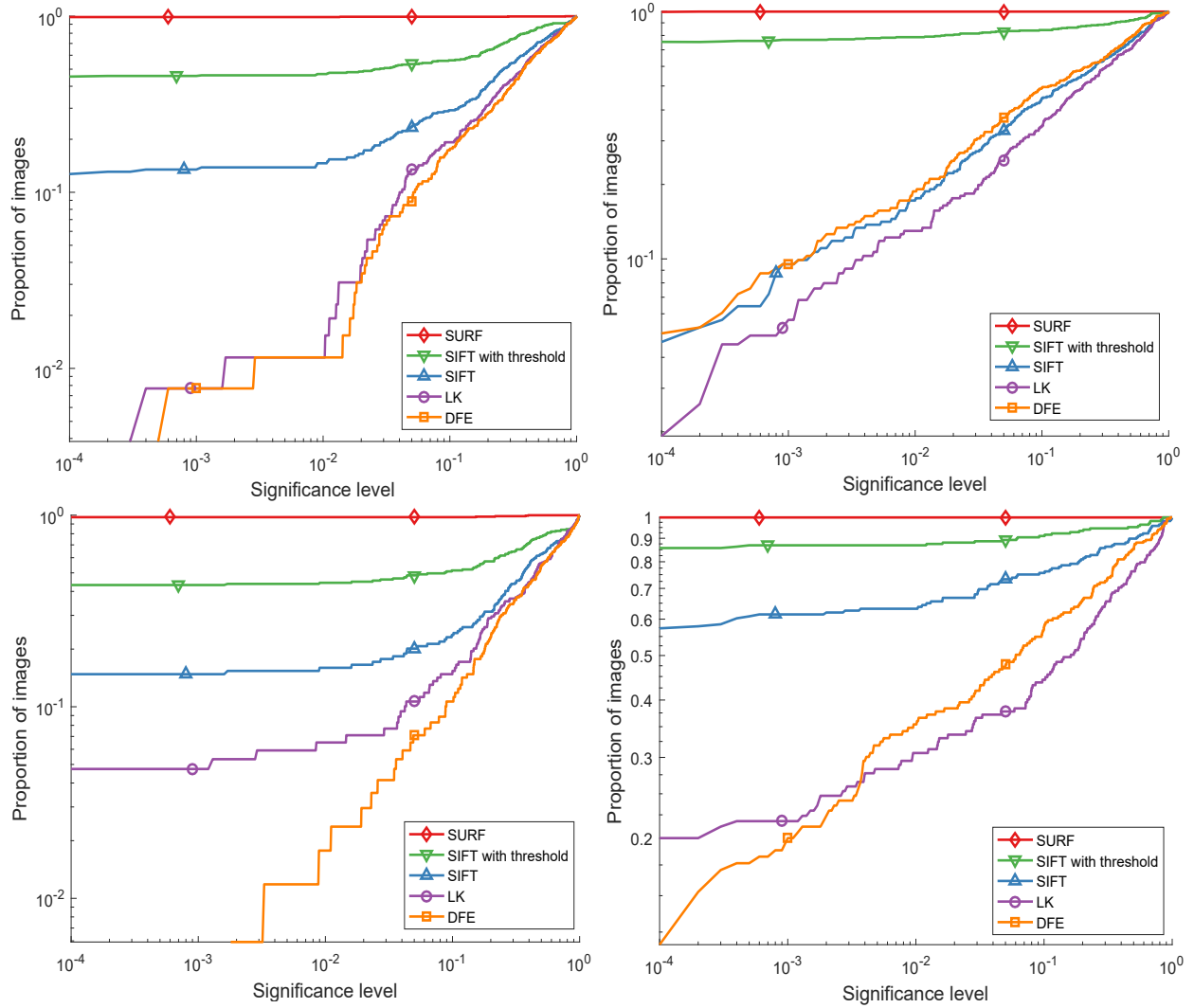


Figure 34: Proportion of images for which the hypothesis that the error is due to human labelling of the ground truth can be rejected at the significance level for tracking the face mole under static conditions (top-left), nose tip under static conditions (top-right), face mole under bike conditions (bottom-left), and nose tip under bike conditions (bottom-right).

References

- Milton Abramowitz and Irene A Stegun. Handbook of mathematical functions with formulas, graphs, and mathematical tables, 1988.
- Yassine Ahmine, Guillaume Caron, El Mustapha Mouaddib, and Fatima Chouireb. Adaptive lucas-kanade tracking. *Image and Vis. Comput.*, 88:1–8, 2019.
- Haldun Akoglu. User's guide to correlation coefficients. *Turkish Journal of Emergency Medicine*, 18(3):91–93, 2018.
- Hesham A Albergy, Abdelfatah A Hegazy, and Gouda I Salama. A fast sift based method for copy move forgery detection. *Future Comput. and Inform. J.*, 3(2):159–165, 2018.
- Matthew Anderson, Ricardo Motta, Srinivasan Chandrasekar, and Michael Stokes. Proposal for a standard default color space for the internet-srgb. In *Color and imaging conference*, volume 1996, pages 238–245. Society for Imaging Science and Technology, 1996.
- Sadaf Ansari. A review on sift and surf for underwater image feature detection and matching. In *2019 IEEE International Conference on Electrical, Computer and Communication Technologies (ICECCT)*, pages 1–4. IEEE, 2019.
- Akram Ashyani, Chi-Lun Lin, Esteban Roman, Ted Yeh, Tachyon Kuo, Wei-Fang Tsai, Yushan Lin, Ric Tu, Austin Su, Chien-Chih Wang, Chun-Hsiang Tan, and Torbjörn E M Nordling. Digitization of updrs upper limb motor examinations towards automated quantification of symptoms of parkinson's disease. *Manuscript in preparation*, 2022.
- Simon Baker, Daniel Scharstein, JP Lewis, Stefan Roth, Michael J Black, and Richard Szeliski. A database and evaluation methodology for optical flow. *Int. J. of Comput. Vis.*, 92(1):1–31, 2011.
- Herbert Bay, Tinne Tuytelaars, and Luc Van Gool. Surf: Speeded up robust features. In *European conference on computer vision*, pages 404–417. Springer, 2006.
- Jeffrey S Beis and David G Lowe. Shape indexing using approximate nearest-neighbour search in high-dimensional spaces. In *Proceedings of IEEE computer society conference on computer vision and pattern recognition*, pages 1000–1006. IEEE, 1997.
- Fangming Bi, Xin Ma, Wei Chen, Weidong Fang, Huayi Chen, Jingru Li, and Biruk Assefa. Review on video object tracking based on deep learning. *J. of New Media*, 1(2):63, 2019.
- Alexey Bochkovskiy, Chien-Yao Wang, and Hong-Yuan Liao. Yolov4: Optimal speed and accuracy of object detection. *arXiv preprint*, 2020.
- Jean-Yves Bouguet. Pyramidal implementation of the affine lucas kanade feature tracker description of the algorithm. *Intel Corporation*, 5(1-10):4, 2001.
- Daniel J Butler, Jonas Wulff, Garrett B Stanley, and Michael J Black. A naturalistic open source movie for optical flow evaluation. In *European conference on computer vision*, pages 611–625. Springer, 2012.
- Che-Han Chang, Chun-Nan Chou, and Edward Y Chang. Clkn: Cascaded lucas-kanade networks for image alignment. In *Proceedings of the IEEE Conference on Computer Vision and Pattern Recognition*, pages 2213–2221, 2017.
- Chien-Chang Chen, Wei-Yu Lu, and Chung-Hsuan Chou. Rotational copy-move forgery detection using sift and region growing strategies. *Multimed. Tools and Appl.*, 78(13):18293–18308, 2019.
- Chun-Hong Cheng, Kwan-Long Wong, Jing-Wei Chin, Tsz-Tai Chan, and Richard HY So. Deep learning methods for remote heart rate measurement: a review and future research agenda. *Sensors*, 21(18):6296, 2021a.
- Yihua Cheng, Hao-fei Wang, Yiwei Bao, and Feng Lu. Appearance-based gaze estimation with deep learning: A review and benchmark. *arXiv preprint arXiv:2104.12668*, 2021b.
- Hsiang-Jen Chien, Chen-Chi Chuang, Chia-Yen Chen, and Reinhard Klette. When to use what feature? sift, surf, orb, or a-kaze features for monocular visual odometry. In *2016 International Conference on Image and Vision Computing New Zealand (IVCNZ)*, pages 1–6. IEEE, 2016.
- Lovish Chum, Anbumani Subramanian, Vineeth N Balasubramanian, and CV Jawahar. Beyond supervised learning: a computer vision perspective. *J. of the Indian Inst. of Sci.*, 99(2):177–199, 2019.
- Joon Son Chung, Andrew Senior, Oriol Vinyals, and Andrew Zisserman. Lip reading sentences in the wild. In *2017 IEEE Conference on Computer Vision and Pattern Recognition (CVPR)*, pages 3444–3453. IEEE, 2017.
- Gioele Ciaparrone, Francisco Luque Sánchez, Siham Tabik, Luigi Troiano, Roberto Tagliaferri, and Francisco Herrera. Deep learning in video multi-object tracking: A survey. *Neurocomputing*, 381:61–88, 2020.
- Philippe Colantoni, Jean-Baptiste Thomas, and Alain Trémeau. Sampling ciela color space with perceptual metrics. *International Journal of Imaging and Robotics*, 16(3):1–22, 2016.
- Jifeng Dai, Yi Li, Kaiming He, and Jian Sun. R-fcn: Object detection via region-based fully convolutional networks. In *Advances in neural information processing systems*, pages 379–387, 2016.
- Alexey Dosovitskiy, Philipp Fischer, Eddy Ilg, Philip Hausser, Caner Hazirbas, Vladimir Golkov, Patrick Van Der Smagt, Daniel Cremers, and Thomas Brox. FlowNet: Learning optical flow with convolutional networks. In *Proceedings of the IEEE international conference on computer vision*, pages 2758–2766, 2015.
- Youssef Douini, Jamal Riffi, Adnane Mohamed Mahraz, and Hamid Tairi. An image registration algorithm based on phase correlation and the classical lucas-kanade technique. *Signal, Image and Video Process.*, 11(7):1321–1328, 2017a.
- Youssef Douini, Jamal Riffi, Mohamed Adnane Mahraz, and Hamid Tairi. Solving sub-pixel image registration problems using phase correlation and lucas-kanade optical flow method. In *2017 Intelligent Systems and Computer Vision (ISCV)*, pages 1–5. IEEE, 2017b.
- Iyad Abu Doush and AL-Btoush Sahar. Currency recognition using a smartphone: Comparison between color sift and gray scale sift algorithms. *J. of King Saud University-Computer and Inf. Sci.*, 29(4):484–492, 2017.
- Vincent Dumoulin and Francesco Visin. A guide to convolution arithmetic for deep learning. *arXiv preprint*, 2018.
- Guangyu Gao, Liling Liu, Li Wang, and Yihang Zhang. Fashion clothes matching scheme based on siamese network and autoencoder. *Multimed. Syst.*, 25(6):593–602, 2019.
- I Garcia, Sebastian Bronte, Luis Miguel Bergasa, Javier Almazán, and J Yebes. Vision-based drowsiness detector for real driving conditions. In *2012 IEEE Intelligent Vehicles Symposium*, pages 618–623. IEEE, 2012.
- Andreas Geiger, Philip Lenz, Christoph Stiller, and Raquel Urtasun. Vision meets robotics: The kitti dataset. *The International Journal of Robotics Research*, 32(11):1231–1237, 2013.

- Ian Goodfellow, Yoshua Bengio, and Aaron Courville. *Deep learning*. MIT Press, Cambridge, MA, U.S.A., 2016. ISBN 978-0262035613. URL <http://www.deeplearningbook.org>.
- Albert Gordo, Jon Almazán, Jerome Revaud, and Diane Larlus. Deep image retrieval: Learning global representations for image search. In *European conference on computer vision*, pages 241–257. Springer, 2016.
- Xifeng Guo, Xinwang Liu, En Zhu, and Jianping Yin. Deep clustering with convolutional autoencoders. In Derong Liu, Shengli Xie, Yuanqing Li, Dongbin Zhao, and El-Sayed M. El-Alfy, editors, *Neural Information Processing*, pages 373–382, Cham, 2017. Springer International Publishing. ISBN 978-3-319-70096-0.
- Amir HajiRassouliha, Andrew J Taberner, Martyn P Nash, and Poul MF Nielsen. Subpixel phase-based image registration using savitzky–golay differentiators in gradient-correlation. *Comput. Vis. and Image Underst.*, 170:28–39, 2018.
- M. A. Hassan, A. S. Malik, D. Fofi, N. Saad, B. Karasfi, Y. S. Ali, and F. Meriaudeau. Heart rate estimation using facial video: A review. *Biomed. Signal Proces. and Control.*, 38: 346–360, 2017. ISSN 17468108.
- K. He, X. Zhang, S. Ren, and J. Sun. Deep residual learning for image recognition. In *2016 IEEE Conference on Computer Vision and Pattern Recognition (CVPR)*, pages 770–778, June 2016. doi: 10.1109/CVPR.2016.90.
- Kaiming He, Georgia Gkioxari, Piotr Dollár, and Ross Girshick. Mask r-cnn. In *Proceedings of the IEEE international conference on computer vision*, pages 2961–2969, 2017a.
- Kaiming He, Georgia Gkioxari, Piotr Dollár, and Ross Girshick. Mask r-cnn. In *Proceedings of the IEEE international conference on computer vision*, pages 2961–2969, 2017b.
- G.E. Hinton and R. R. Salakhutdinov. Reducing the dimensionality of data with neural networks. *Sci.*, 313(July):504–507, 2006.
- Eric B Holmgren. The pp plot as a method for comparing treatment effects. *J. of the Am. Stat. Assoc.*, 90(429):360–365, 1995.
- Berthold KP Horn and Brian G Schunck. Determining optical flow. In *Techniques and Applications of Image Understanding*, volume 281, pages 319–331. International Society for Optics and Photonics, 1981.
- Borui Hou and Ruqiang Yan. Convolutional autoencoder model for finger-vein verification. *IEEE Transactions on Instrumentation and Measurement*, 69(5):2067–2074, 2019.
- Abdullah Ayub Khan, Asif Ali Laghari, and Shafique Ahmed Awan. Machine learning in computer vision: A review. *EAI Trans. on Scalable Inf. Syst.*, page e4, 2021.
- Nabeel Khan, Brendan McCane, and Steven Mills. Better than sift? *Mach. Vis. and Appl.*, 26(6):819–836, 2015.
- Diederik P Kingma and Jimmy Ba. Adam: A Method for Stochastic Optimization. *arXiv preprint*, pages 1–15, 2014. ISSN 09252312.
- Vladimir A Knyaz, Oleg Vygolov, Vladimir V Kniaz, Yuri Vizilter, Vladimir Gorbatshevich, Thomas Luhmann, and Niklas Conen. Deep learning of convolutional auto-encoder for image matching and 3d object reconstruction in the infrared range. In *Proceedings of the IEEE International Conference on Computer Vision Workshops*, pages 2155–2164, 2017.
- H Law and J Deng. Detecting objects as paired keypoints. *Lect. Notes in Comput. Sci.*, pages 765–781, 2018.
- Yann LeCun, Koray Kavukcuoglu, and Clément Farabet. Convolutional networks and applications in vision. In *Proceedings of 2010 IEEE international symposium on circuits and systems*, pages 253–256. IEEE, 2010.
- Wookey Lee, Jessica Jiwon Seong, Busra Ozlu, Bong Sup Shim, Azizbek Marakhimov, and Suan Lee. Biosignal sensors and deep learning-based speech recognition: A review. *Sensors*, 21(4):1399, 2021.
- Tsung-Yi Lin, Michael Maire, Serge Belongie, James Hays, Pietro Perona, Deva Ramanan, Piotr Dollár, and C Lawrence Zitnick. Microsoft coco: Common objects in context. In *European conference on computer vision*, pages 740–755. Springer, 2014.
- Tsung-Yi Lin, Piotr Dollár, Ross Girshick, Kaiming He, Bharath Hariharan, and Serge Belongie. Feature pyramid networks for object detection. In *Proceedings of the IEEE conference on computer vision and pattern recognition*, pages 2117–2125, 2017a.
- Tsung-Yi Lin, Priya Goyal, Ross Girshick, Kaiming He, and Piotr Dollár. Focal loss for dense object detection. In *Proceedings of the IEEE international conference on computer vision*, pages 2980–2988, 2017b.
- Li Liu, Wanli Ouyang, Xiaogang Wang, Paul Fieguth, Jie Chen, Xinwang Liu, and Matti Pietikäinen. Deep learning for generic object detection: A survey. *International Journal of Computer Vision*, 128(2):261–318, 2020.
- Wei Liu, Dragomir Anguelov, Dumitru Erhan, Christian Szegedy, Scott Reed, Cheng-Yang Fu, and Alexander C Berg. Ssd: Single shot multibox detector. In *European conference on computer vision*, pages 21–37. Springer, 2016.
- David G. Lowe. Distinctive image features from scale-invariant keypoints. *Int. J. of Comp. Vis.*, 60(2):91–110, 2004. ISSN 09205691.
- Bruce Lucas and Takeo Kanade. An iterative image registration technique with an application to stereo vision. In *IJCAI*, volume 81, 04 1981.
- Ilja Manakov, Markus Rohm, and Volker Tresp. Walking the tightrope: an investigation of the convolutional autoencoder bottleneck. *arXiv preprint*, 2019.
- Francesca Manni, Fons van der Sommen, Svitlana Zinger, Caifeng Shan, Ronald Holthuisen, Marco Lai, Gustav Buström, Richelle JM Hoveling, Erik Edström, Adrian Elmi-Terander, et al. Hyperspectral imaging for skin feature detection: Advances in markerless tracking for spine surgery. *Applied Sciences*, 10(12):4078, 2020.
- K McLaren. Xiii—the development of the cie 1976 ($L^* a^* b^*$) uniform colour space and colour-difference formula. *J. of the Soc. of Dyers and Colour.*, 92(9):338–341, 1976.
- Krystian Mikolajczyk and Cordelia Schmid. A performance evaluation of local descriptors. *IEEE transactions on pattern analysis and machine intelligence*, 27(10):1615–1630, 2005.
- Hartmut Neven, Geordie Rose, and William G Macready. Image recognition with an adiabatic quantum computer i. mapping to quadratic unconstrained binary optimization. *arXiv preprint arXiv:0804.4457*, 2008.
- Aoxin Ni, Arian Azarang, and Nasser Kehtarnavaz. A review of deep learning-based contactless heart rate measurement methods. *Sensors*, 21(11):3719, 2021.
- Hyeonwoo Noh, Andre Araujo, Jack Sim, Tobias Weyand, and Bohyung Han. Large-scale image retrieval with attentive deep local features. In *Proceedings of the IEEE international conference on computer vision*, pages 3456–3465, 2017.

- Xiaorong Pu, Ke Fan, Xiong Chen, Luping Ji, and Zhihu Zhou. Facial expression recognition from image sequences using twofold random forest classifier. *Neurocomputing*, 168:1173–1180, 2015.
- Joseph Redmon and Ali Farhadi. Yolo9000: better, faster, stronger. In *Proceedings of the IEEE conference on computer vision and pattern recognition*, pages 7263–7271, 2017.
- Joseph Redmon and Ali Farhadi. Yolov3: An incremental improvement. *arXiv preprint*, 2018.
- Joseph Redmon, Santosh Divvala, Ross Girshick, and Ali Farhadi. You only look once: Unified, real-time object detection. In *Proceedings of the IEEE conference on computer vision and pattern recognition*, pages 779–788, 2016.
- Shaoqing Ren, Kaiming He, Ross Girshick, and Jian Sun. Faster r-cnn: Towards real-time object detection with region proposal networks. In *Advances in neural information processing systems*, pages 91–99, 2015.
- Rasmus Rothe, Radu Timofte, and Luc Van Gool. Deep expectation of real and apparent age from a single image without facial landmarks. *Int. J. of Comp. Vis.*, 126(2-4):144–157, 2018.
- Paul-Edouard Sarlin, Daniel DeTone, Tomasz Malisiewicz, and Andrew Rabinovich. Superglue: Learning feature matching with graph neural networks. In *Proceedings of the IEEE/CVF conference on computer vision and pattern recognition*, pages 4938–4947, 2020.
- Gulbadan Sikander and Shahzad Anwar. Driver fatigue detection systems: A review. *IEEE Transactions on Intelligent Transportation Systems*, 20(6):2339–2352, 2018.
- Edgar Simo-Serra, Eduard Trulls, Luis Ferraz, Iasonas Kokkinos, Pascal Fua, and Francesc Moreno-Noguer. Discriminative learning of deep convolutional feature point descriptors. In *Proceedings of the IEEE international conference on computer vision*, pages 118–126, 2015.
- Marzuraikah Mohd Stofa, Mohd Asyraf Zulkifley, and Muhammad Ammirul Atiqi Mohd Zainuri. Skin lesions classification and segmentation: A review. *International Journal of Advanced Computer Science and Applications*, 12(10), 2021.
- Peifeng Su, Daizhi Liu, Xihai Li, and Zhigang Liu. A saliency-based band selection approach for hyperspectral imagery inspired by scale selection. *IEEE Geoscience and Remote Sensing Letters*, 15(4):572–576, 2018.
- Jiaming Sun, Zehong Shen, Yuang Wang, Hujun Bao, and Xiaowei Zhou. Loftr: Detector-free local feature matching with transformers. In *Proceedings of the IEEE/CVF conference on computer vision and pattern recognition*, pages 8922–8931, 2021.
- Christian Szegedy, Liu Wei, Jia Yangqing, Sermanet Pierre, Reed Scott, Anguelov Dragomir, Erham Dumitru, Vanhoucke Vincent, and Rabinovich Andrew. Inception-v4, Inception-ResNet and the Impact of Residual Connections on Learning. *Popul. Health Manag.*, 18(3):186–191, 2015. ISSN 1942-7891. doi: 10.1089/pop.2014.0089. URL <http://online.liebertpub.com/doi/10.1089/pop.2014.0089>.
- Shaharyar Ahmed Khan Tareen and Zahra Saleem. A comparative analysis of sift, surf, kaze, akaze, orb, and brisk. In *2018 International conference on computing, mathematics and engineering technologies (iCoMET)*, pages 1–10. IEEE, 2018.
- Jose Miguel Tarongi and Adriano Camps. Normality analysis for rfi detection in microwave radiometry. *Remote Sensing*, 2(1):191–210, 2010.
- George Brinton Thomas and Ross L Finney. *Calculus And Analytic Geometry*. Addison-Wesley Publishing Company, 1900 E Lake Ave Glenview, IL 60025 United States, 1961.
- Quoc-Viet Tran, Shun-Feng Su, and Van-Truong Nguyen. Pyramidal lucas-kanade-based noncontact breath motion detection. *IEEE Transactions on Systems, Man, and Cybernetics: Systems*, 50(7):2659–2670, 2018.
- Marco C. Uchida, Renato Carvalho, Vitor Daniel Tessutti, Reury Frank Pereira Bacurau, Hélio José Coelho-Júnior, Luciane Portas Capelo, Heloiza Prando Ramos, Marcia Calixto dos Santos, Luís Felipe Milano Teixeira, and Paulo Henrique Marchetti. Identification of muscle fatigue by tracking facial expressions. *PLoS ONE*, 13(12):1–11, 2018. ISSN 19326203.
- Ashish Vaswani, Noam Shazeer, Niki Parmar, Jakob Uszkoreit, Llion Jones, Aidan N Gomez, Lukasz Kaiser, and Illia Polosukhin. Attention is all you need. In *Advances in neural information processing systems*, pages 5998–6008, 2017.
- Chien-Chih Wang. Non-contact heart rate measurement based on facial videos. Master’s thesis, National Cheng Kung University, No. 1, Dasyue Rd, East District, Tainan City, 701, 2020.
- Nannan Wang, Xinbo Gao, Dacheng Tao, Heng Yang, and Xuelong Li. Facial feature point detection: A comprehensive survey. *Neurocomputing*, 275:50–65, 2018. ISSN 18728286.
- Philippe Weinzaepfel, Jerome Revaud, Zaid Harchaoui, and Cordelia Schmid. Deepflow: Large displacement optical flow with deep matching. In *Proceedings of the IEEE international conference on computer vision*, pages 1385–1392, 2013.
- Xue Iuan Wong and Manoranjan Majji. Uncertainty quantification of lucas kanade feature track and application to visual odometry. In *2017 IEEE Conference on Computer Vision and Pattern Recognition Workshops (CVPRW)*, pages 950–958. IEEE, 2017.
- Jure Zbontar and Yann LeCun. Stereo matching by training a convolutional neural network to compare image patches. *J. of Mach. Learn. Res.*, 17(1):2287–2318, 2016.
- Matthew D Zeiler, Dilip Krishnan, Graham W Taylor, and Rob Fergus. Deconvolutional networks. In *2010 IEEE Computer Society Conference on computer vision and pattern recognition*, pages 2528–2535. IEEE, 2010.
- Zhifei Zhang, Yang Song, and Hairong Qi. Age progression/regression by conditional adversarial autoencoder. In *IEEE Conference on Computer Vision and Pattern Recognition (CVPR)*. IEEE, 2017.
- Amy Zhao, Frédo Durand, and John Guttag. Estimating a small signal in the presence of large noise. In *Proceedings of the IEEE International Conference on Computer Vision*, volume 2016-Febru, pages 671–676, 2016. ISBN 9781467383905.
- Jianqing Zhao, Xiaohu Zhang, Chenxi Gao, Xiaolei Qiu, Yongchao Tian, Yan Zhu, and Weixing Cao. Rapid mosaicking of unmanned aerial vehicle (uav) images for crop growth monitoring using the sift algorithm. *Remote. Sens.*, 11(10):1226, 2019.
- Liang Zheng, Yi Yang, and Qi Tian. Sift meets cnn: A decade survey of instance retrieval. *IEEE transactions on pattern analysis and machine intelligence*, 40(5):1224–1244, 2017.
- Yan-Tao Zheng, Ming Zhao, Yang Song, Hartwig Adam, Ulrich Buddemeier, Alessandro Bissacco, Fernando Brucher, Tat-Seng Chua, and Hartmut Neven. Tour the world: building a web-scale landmark recognition engine. In *2009 IEEE Conference on Computer Vision and Pattern Recognition*, pages 1085–1092. IEEE, 2009.

Xingyi Zhou, Dequan Wang, and Philipp Krähenbühl. Objects as points. *arXiv preprint arXiv:1904.07850*, 2019.